Earth-Science Reviews 218 (2021) 103667

Contents lists available at ScienceDirect

Earth-Science Reviews

journal homepage: www.elsevier.com/locate/earscirev

The epicentral fingerprint of earthquakes marks the coseismically activated crustal volume

P. Petricca [a], C. Bignami [b], C. Doglioni [a,b,*]

[a] Dipartimento di Scienze della Terra, Sapienza University, Rome, Italy
[b] Istituto Nazionale di Geofisica e Vulcanologia, Rome, Italy

ARTICLE INFO

Keywords:
InSAR coseismic vertical deformation
Earthquake epicentral area
Near-field active domain
Seismic hazard assessment
Constructive waves inferference

ABSTRACT

InSAR images allow to detect the coseismic deformation, delimiting the epicentral area where the larger displacement has been concentrated. By inspecting the InSAR fringe patterns it is commonly recognized that, for dip-slip faults, the most deformed area is elliptical, or quadrilobated for strike-slip faults. This area coincides with the surface projection of the volume coseismically mobilized in the hanging wall of thrusts and normal faults, or the crustal walls adjacent to strike-slip faults. In the present work we analyzed a dataset of 32 seismic events, aiming to compare the deformation fields in terms of shape, spatial extents, and amount of deformed rock volumes, and the corresponding earthquake type and magnitudes. The dimension of the deformed area detected by InSAR scales with the magnitude of the earthquake, and we found that for $M \geq 6$ is always larger than 100 km^2, increasing to more than 550 km^2 for $M \approx 6.5$. Moreover, the comparison between InSAR and Peak Ground Accelerations documents the larger shaking within the areas suffering higher vertical deformation. As well established, the seismic epicenter rarely coincides with the area of larger shaking. Instead, the higher macroseismic intensity often corresponds to the area of larger vertical displacement (either downward or upward), apart local site amplification effects. Outside this area, the vertical displacement is drastically lower, determining the strong attenuation of seismic waves and the decrease of the peak ground acceleration in the surrounding far-field area. Indeed, the segment of the activated fault constrains the area where the vertical oscillations are larger, allowing the contemporaneous maximum freedom degree of the crustal volume affected by horizontal maximum shaking, i.e., the near-field or epicentral area; therefore, the epicentral area and volume are active, i.e., they coseismically move and are contemporaneously crossed by seismic waves (active volume and surface active domain) where trapped waves and constructive interference are expected, whereas the surrounding far-field area is mainly fixed and passively crossed by seismic waves (passive volume and surface passive domain). All these considerations point out that InSAR images of areas affected by earthquakes are a powerful tool representing the fingerprint of the epicentral area where the largest shaking has taken place during an earthquake. Seismic hazard assessments should primarily rely on the expected future active domains.

1. Introduction

The earthquake source is a common term to identify the area or volume affected by the rupture on the fault plane where seismic body waves are generated and radiated outwards, whereas the source location is given as the hypocenter where fault rupture initiates at depth, or focal depth, and the epicenter is the surface vertical projection of the hypocenter (e.g., Stein and Wysession, 2009; Bath, 2013; Scholz, 2019; Bormann and Saul, 2020). The epicentral area is usually assumed to represent the zone of largest shaking and damage, also called near-field, in contrast with the far-field where shaking is less severe due to the energy dissipation governed by the anelasticity parameters and the increase of the involved crustal volume. The deformation of the ground around the fault activated during an earthquake can be described by a dislocation in an elastic half space (e.g., Kanamori, 1973; Okada, 1985), regardless the source energy, which is elastic for thrust and strike-slip faults, whereas it is gravitational for normal faults (Doglioni et al., 2011, 2015a, 2015b; Bignami et al., 2020; Albano et al., 2021a, 2021b). According to Shearer (2019), assuming a spherical symmetric waveform, the near-field represents the permanent static displacement due to

* Corresponding author at: Istituto Nazionale di Geofisica e Vulcanologia, Rome, Italy.
E-mail address: carlo.doglioni@uniroma1.it (C. Doglioni).

https://doi.org/10.1016/j.earscirev.2021.103667
Received 8 February 2021; Received in revised form 4 May 2021; Accepted 5 May 2021
Available online 7 May 2021

the source and mostly decays as $1/r^2$, where r is the distance from the source, since it is important only relatively close to the epicenter. The near-field is conventionally attributed to an undefined radial distance from the epicenter and the source fault. Moreover, due to directivity of the rupture propagation (Calderoni et al., 2017), sub-events migration (e.g., Yao et al., 2012; Yue and Lay, 2020) and site amplification effects (e.g., Milana et al., 2019), the strongest macroseismic intensity does not often rely on the epicenter or in a restricted area. An example is the bridge collapsed in Oakland, far away from the fault strike and about 70 km from the epicenter, due to site amplification associated with the 1989 Loma Prieta M 6.9 earthquake in California (Beaudouin et al., 1994). In the near-field, vertical and horizontal stronger ground motion concur and the ratio of the maximum vertical spectral response to the horizontal can exceed one at very short periods (0.15 s) but falls off rapidly with period reaching a value of about 0.5 for long periods (Ambraseys and Douglas, 2003). For example, it was shown that in extensional tectonic regimes, the highest macroseismic intensity largely corresponds to the area that underwent the strongest coseismic subsidence (Liberatore et al., 2019) and vertical jerks can explain the largest damage (Mariani and Pugi, 2020). Nowadays, the displacement and deformation in the epicentral area can be analyzed by a number of classic and new techniques such as strong-motion data, Global Navigation Satellite System (GNSS) and Interferometric Synthetic Aperture Radar (InSAR), and also by forward modelling. Indeed, coseismic surface deformation can be obtained by dislocation theory of an elastic medium as shown by Okada (1985, 1992), where the affected area is the combination of the fault dislocation and its upward propagation through the medium, and it depends on the dip and depth of the assumed activated main fault plane. It is worth to note that not accurate estimation of fault parameters (especially in poorly instrumented areas) cannot provide reliable information about the affected areas (Bignami et al., 2021). Where present, GNSS stations provide excellent measuring of the horizontal and vertical components of the coseismic movements of the single sites (e.g., Anzidei et al., 2009; Wilkinson et al., 2017; Guglielmino et al., 2013). However, they cannot precisely cover the whole deformed area. In this article we discuss the powerful information resulting from InSAR data in describing the area affected by deformation during an earthquake, providing a tool for better understanding the near-field and far-field distinction, based on the geological control of the seismological signatures. This analysis also provides a tool for better seismic hazard assessment that should focus specifically on the near-field shaking, contributing to the enhancement of techniques on seismic hazard evaluation (e.g., Panza et al., 2014; Dall'Asta et al., 2021).

1.1. The InSAR and earthquake fingerprints

Since the first 'photography' of the deformation generated by the Landers earthquake was recorded (Massonnet et al., 1993) thanks to InSAR, a long list of seismic events has been analyzed during the years by the increasing number of satellites and the improved quality of SAR sensors and InSAR techniques in continental areas (Biggs and Wright, 2020). Synthetic Aperture Radar (SAR) sensors and SAR interferometry (InSAR, e.g., Massonnet and Feigl, 1995) have widely demonstrated the capability to detect and measure ground deformation induced by earthquakes. InSAR measures displacement, but considering the concave shape of the coseismic ground modification (i.e., the progressive strain accumulated by a graben or an anticline), this can be defined as a crustal deformation. McGarr (1999) suggests that earthquakes have a seismic efficiency of 6%, and the question is where the remaining 94% is dissipated; apart from shear heating, most of the deformation must be consumed in fracturing and deforming the upper crust (Doglioni et al., 2015a), which may assume elongated sags in the hanging wall of normal faults (Bignami et al., 2019). Seismic radiation has near-field terms, which decay rapidly with distance from an exciting earthquake and include static terms. They are important to the strong ground motion near to an earthquake (Stacey and Davis, 2008).

InSAR is nowadays routinely applied to study coseismic surface effects, making available dense information on the amount of occurred deformation and on the extent of the impacted areas. Moreover, the interferograms can figure out also the earthquake mechanisms, thanks to the property to map the shape and the spatial distribution of the ground deformation. The interferograms (or the corresponding topographic change map) can provide a sort of fingerprint of the analyzed earthquakes. In other words, such fingerprints offer a new perspective to define the epicentral area, not only by means of the radial distance with respect to the earthquake epicenter, but also by delineating the actual region affected by deformation.

Integrating InSAR images, seismological and accelerometric data we extract important information that characterizes an earthquake: the amount of deformed area, the corresponding involved crustal volume, the concentration of vertical and horizontal shaking. These values can be expressed as a function of the event magnitudes. We scrutinize a list of 32 moderate to major earthquakes as a function of their tectonic setting, magnitude, dimension of the deformed area and ground shaking (Fig. 1 and Table 1). The aim is to recognize how these parameters correlate and to provide a key to accurately identify the epicentral or near-field area.

2. Materials and Methods

2.1. InSAR and seismological data selection

The earthquakes selected in the present study have the following requirements: i) both the InSAR deformation data and the seismological data of the earthquakes are available; ii) SAR data are provided in the literature (e.g., as auxiliary material or public databases) or the figure describing the deformation pattern in the corresponding paper is readable (i.e., deformation fringes are traceable) and correctly georeferenced. Events related to plate margin tectonics (e.g., megathrusts or mid-oceanic ridges) are excluded because the displacement pattern is mostly offshore and no InSAR data are available.

Coseismic fringes (or measured deformation) illuminated by SAR images were georeferenced in a geographic information system (QGis software, version 2.8.6). Areas interested by displacement, were then manually delimited by polygons that are used to calculate the area of the surface affected by deformation (see Table 1 and Figs. 2–4). Each event of our dataset and related references is described by geographic (longitude, latitude and focal depth), geometric (strike, dip) and kinematic (rake) parameters obtained from the literature (Table 1) or, if not given, from earthquake regional databases (National Earthquake Observatory of INGV for Italy, National Observatory of Athens for Greece, KOERI catalogue for Turkey, USGS catalogue for U.S. and worldwide), and the coseismic maximum displacement (either total or, where not present, the maximum along a single Line-Of-Sight or LOS). From the same seismic catalogs we extracted the whole instrumental seismicity affecting the volume of the crust underlying the region deformed during the coseismic phase of the selected event. The deepest depth of recorded events may be used to define the maximum seismogenic depth at that location. The maximum depth of seismicity is used to a rough estimate of the volume coseismically mobilized during the earthquake sequence. For normal and thrust fault events (geometrically is not quantifiable for strike-slip faults), the volume is calculated considering the deformed area as the base of an inverted prism with the vertex at the maximum seismogenic depth ($V = 1/2*A*zmax$; where A is the deformed area and zmax is the maximum seismogenic depth). It is necessary to consider the depth values provided by seismic catalogs with caution for some reasons. First of all, events analyzed in this study are in many cases dated events or in poorly studied areas, i.e. the recording networks in such areas are very sparse. The first imply that most events have an imposed depth especially for shallow earthquakes (e.g., USGS, 2018) or a location-specific value statistically derived from past events (e.g., Bondar and Storchak, 2011). The latter assumption is even common in

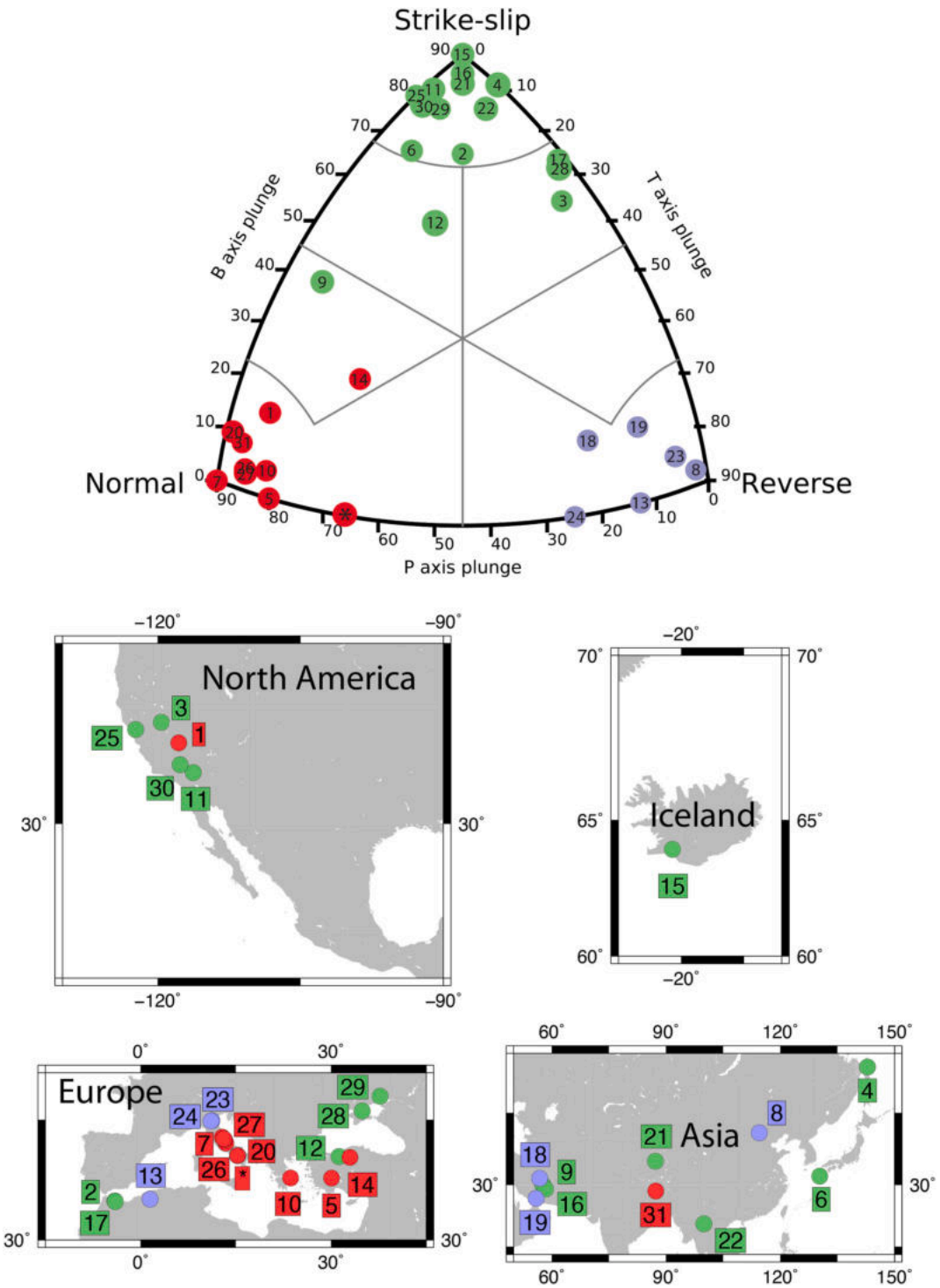

Fig. 1. Classification according to focal mechanism (upper panel) plotted with the FMC routine (Álvarez-Gómez, 2019) and distribution of the studied earthquakes. Red, normal faults; light blue, thrusts; green, strike-slip faults. See list in Table 1. (For interpretation of the references to colour in this figure legend, the reader is referred to the web version of this article.)

countries with dense seismic networks where free-depth solutions are sacrificed to better localize the event. In the case of free-depth solutions exist disproportionately large depth errors (up to 200 km for a 5 km deep event; see Nievas et al., 2020). Furthermore, information on error associated with the depth calculations are often not provided in seismic catalogs. These epistemic uncertainties make it impossible to have a high confidence in seismic volumes, which calculation is just based on the depth of seismicity.

2.2. PGA data selection

Italy has one of the best developed accelerometric networks operating since 1972 and constantly improved in number of stations and in terms of quality of recorded data, also following the numerous moderate to large earthquakes affecting the whole territory.

Analyzed waveforms are mainly recorded by the Italian National Accelerometric Network (RAN) and National Seismic Network (RSN)

Table 1
Parameters of the 32 moderate-strong-major seismic events analyzed in this study. ID*, normal fault M 6.9 Irpinia 1980 area has been computed by geodetic leveling, since SAR technique was not available. N/A, not available; LOS, data limited only on the displacement recorded on the light-of-sight.

ID	date	location	longitude	latitude	Mw	depth	strike	dip	rake	type	deformation area (km^2)	max seismogenic depth (km)	max up or *positive LOS (mm)	max down or *negative LOS (mm)	main references
1	17 May 1993	Eureka Valley (California)	242.21	37.11	6.1	9.2	173	54	-109	NN	315	9.2	N/A	*90	Massonnet and Feigl, 1995; Weston et al., 2012
2	26 May 1994	Al Hoceima (Morocco)	355.94	35.2	6	7	24	70	0	SS	204	N/A	*70	*50	Akoglu et al., 2006
3	12 September 1994	Pine Nut Mountains (Nevada)	240.38	38.82	5.9	7.9	319	72	152	SS	229	11.6	*25	*85	Amelung and Bell, 2003
4	27 May 1995	Sakhalin (Russia)	142.9	52.89	7.6	7.3	198	84	174	SS	3907	N/A	*820	N/A	Tobita et al., 1998
5	1 October 1995	Dinar (Turkey)	30.08	38.1	6.1	6.4	145	35	−90	NN	267	15	N/A	*590	Fukahata and Wright, 2008
6	26 March 1997	Kagoshima (Japan)	130.35	31.97	6.1	8	275	81	−19	SS	975	N/A	350	600	Fujiwara et al., 1998
7	26 July 1997	Colfiorito (Italy)	12.85	43.01	6	4.5	144	45	−90	NN	135	19.1	N/A	*240	Hernandez et al., 2004; Salvi et al., 2000; Stramondo et al., 1999
8	10 January 1998	Zhangbei (China)	114.51	41.13	5.7	5	200	43	86	TH	80	10	*115	N/A	Li et al., 2008
9	14 March 1998	Fandoqa (Iran)	57.64	30.01	6.6	3.7	150	52	−146	SS	1223	N/A	N/A	N/A	Berberian et al., 2001
10	7 September 1999	Athens (Greece)	23.63	38.11	5.9	9.5	116	54	−84	NN	231	20	N/A	*56	Kontoes et al., 2000
11	16 October 1999	Hector Mine (California)	243.73	34.56	7.1	6.1	332	83	185	SS	2637	N/A	*1000	*800	Jónsson et al., 2002
12	12 November 1999	Duzce (Turkey)	31.26	40.72	7.5	6.8	85	57	−174	SS	3361	N/A	*200	*75	Burgmann et al., 2002
13	27 December 1999	Ain Temouchent (Algeria)	−1.25	35.24	5.7	10	57	32	90	TH	150	10	*80	N/A	Belabbès et al., 2009
14	6 June 2000	Cankiri (Turkey)	32.99	40.63	6	5.5	2	33	−37	NN	232	20	N/A	*150	Cakir and Akoglu, 2008
15	21 June 2000	South Iceland (Iceland)	339.3	63.99	6.5	4.1	0	90	180	SS	915	N/A	*150	*120	Pedersen et al., 2003
16	26 December 2003	Bam (Iran)	58.35	29.05	6.6	5.8	359	86	−180	SS	1857	N/A	*140	*100	Peyret et al., 2007
17	24 February 2004	Al Hoceima (Morocco)	356.01	35.12	6.4	7	335	73	160	SS	530	N/A	*150	*110	Akoglu et al., 2006
18	22 February 2005	Zarand (Iran)	56.8	31.5	6.4	4.6	266	67	105	TH	625	20	*400	*450	Talebian et al., 2006
19	27 November 2005	Qeshm (Iran)	55.89	26.88	5.8	6	73	36	66	TH	232	18	260	N/A	Nissen et al., 2010
20	6 April 2009	L'Aquila (Italy)	13.43	42.32	6.3	7	133	47	−103	NN	318	19.7	40	280	Atzori et al., 2009; Stramondo et al., 2010
21	13 April 2010	Yushu (China)	96.84	33.06	6.8	7	300	84	0	SS	2026	N/A	270	400	Wang et al., 2014
22	24 March 2011	Tarlay (Myanmar)	99.94	20.71	6.8	13.2	69	86	11	SS	1849	N/A	*262	*236	Wang et al., 2015
23	20 May 2012	Emilia (Italy)	11.23	44.89	5.9	6	114	40	80	TH	257	19.5	*160	N/A	Tizzani et al., 2013
24	29 May 2012	Emilia (Italy)	11.09	44.85	5.8	5	97	20	90	TH	159	19.2	*140	N/A	Tizzani et al., 2013
25	24 August 2014	Napa Valley (California)	237.69	38.22	6	11	155	82	−172	SS	452	N/A	50	30	Polcari et al., 2017
26	24 August 2016	Amatrice (Italy)	13.23	42.7	6.1	8	161	50	−85	NN	211	18.4	N/A	*200	Cheloni et al., 2017; Lavecchia et al., 2016
27	30 October 2016	Norcia (Italy)	13.11	42.83	6.5	9.2	160	40	−95	NN	549	19.7	120	1000	

(*continued on next page*)

Table 1 (*continued*)

ID	date	location	longitude	latitude	Mw	depth	strike	dip	rake	type	deformation area (km^2)	max seismogenic depth (km)	max up or *positive LOS (mm)	max down or *negative LOS (mm)	main references
28	12 November 2017	Kermanshah (Iran)	34.91	45.96	7.3	11.6	351	73	22	SS	2376	N/A	*918	*488	Cheloni et al., 2017; Valerio et al., 2018; Bignami et al., 2019 Kuang et al., 2019; Monterroso et al., 2020
29	7 November 2019	East Azerbaijan (Iran)	37.74	47.55	5.9	5	29	79	−4	SS	317	N/A	*70	*40	Valerio et al., 2020
30	6 July 2019	Ridgecrest (California)	242.35	35.25	7.1	8	332	80	−173	SS	2250	N/A	*780	*780	Monterroso et al., 2020; Polcari et al., 2021 GEOSAR laboratory INGV
31	20 March 2020	Xigaze (Tibet)	87.31	28.59	5.7	13.5	343	49	−101	NN	54	13.5	N/A	170	
*	23 November 1980	Irpinia (Italy)	15.28	40.84	6.9	10	306	69	270	NN	563	17	N/A	1600	Galli and Peronace, 2014

and freely provided for downloading by the ITACA v3.1 web archive (itaca.mi.ingv.it; D'Amico et al., 2020). Data include ground motion distribution of the seismic events in terms of Peak Ground Acceleration (PGA) and Peak Ground Velocity (PGV) with horizontal and vertical components, plus information about the soil category (NTC18 soil category – Italian Seismic Code, NTC 2018; Iervolino et al., 2018) under the installation point of the various recording stations.

We get PGA horizontal (north and east) and vertical components from the ITACA dataset covering seismic events affecting Italy.

3. Results

We calculated the area affected by the most severe deformation inferred from InSAR coseismic ground deformation data, excluding the surrounding zones where the motion is lower than one single interferometric fringe or within the error of measure (Figs. 2–4). This approach means that we have an accuracy in the delineation of the deformed areas of about half InSAR fringe, that in turn gives a figure of the displacement associated to the outer most fringe of the interferograms. This accuracy depends on the SAR wavelength used to generate the interferograms: for C-band, we have an error in the SAR Line-Of-Sight (LOS) of about 1.4 cm (one fringe is half of the wavelength). At X-band it is about 0.75 cm (note that none of the earthquakes in our list is studied with X-band SAR), and at L-band half fringe is about 5.7 cm. Considering i) the magnitude of the events that we are analyzing (higher than magnitude 5.7 that induce quite large deformation); ii) the amount of displacement itself: half fringe is abundantly less than 10% of the entire rock volume displaced also for lower magnitude events, and iii) that we are looking at the outer fringe of the interferograms, where smaller displacements occur, we can assume that the delineated areas correspond at least to the 90% of the involved rock volume.

We analyzed images from the three main tectonic settings, i.e., extensional, contractional and strike-slip available in the literature (Fig. 1 and Table 1). Events span in the period ranging between 1993 and 2020 plus one event in 1980 and are represented by 32 earthquakes due to normal fault (10 events, Fig. 2), thrust fault (6 events, Fig. 3) and strike slip fault (16 events, Fig. 4). The selected dataset has been supplemented by one earthquake occurred before the advent of SAR technology (M 6.9, 1980 Irpinia – Southern Italy, normal fault earthquake, Galli and Peronace, 2014) studied in detail by means of macroseismic data and geodetic leveling. The coseismic ground deformation illuminated by InSAR data is not surrounding the epicenter in a circular pattern, but it is rather regularly elliptical in normal fault and thrust tectonic settings (Figs. 2, 3) or quadrilobated in strike-slip earthquakes (Fig. 4), being elongated, parallel and adjacent to the activated fault system. The maps depicting the coseismic fringes (or measured deformation) for the 32 selected earthquakes were then used to calculate the area of the surface affected by deformation during the coseismic phase (Table 1 and Figs. 2–4). We consider areas interested by subsidence (or negative LOS when only single orbit data is available), uplift (or positive LOS when only single orbit data is available) and both of them for normal, thrust and strike-slip faults respectively. A simple statistical best fit analysis deformed area versus magnitude may help appreciating the results. In Fig. 5 we show the comparison between these values and the recorded magnitudes. All the events clearly show that deformed areas increase by increasing the magnitudes. The plots highlight the different trends as a function of the earthquake mechanisms since thrust and normal fault earthquakes have a gentler curvature than strike-slip ones (Fig. 5). Taking Mw 6.5 as reference magnitude, the elongated fingerprint of the near-field appears larger for strike-slip faults (≈1000 km^2), with respect to thrusts (≈650 km^2) and normal faults (≈400 km^2). Usually (e.g., Keylis-Borok and Malinovskaya, 1964; Bath and Duda, 1964; Bak et al., 2002) earthquake magnitude is considered proportional to the logarithm of the earthquake source area.

Considering the InSAR fingerprints as the surface projection of the mobilized seismogenic volume, the volume can be estimated for normal

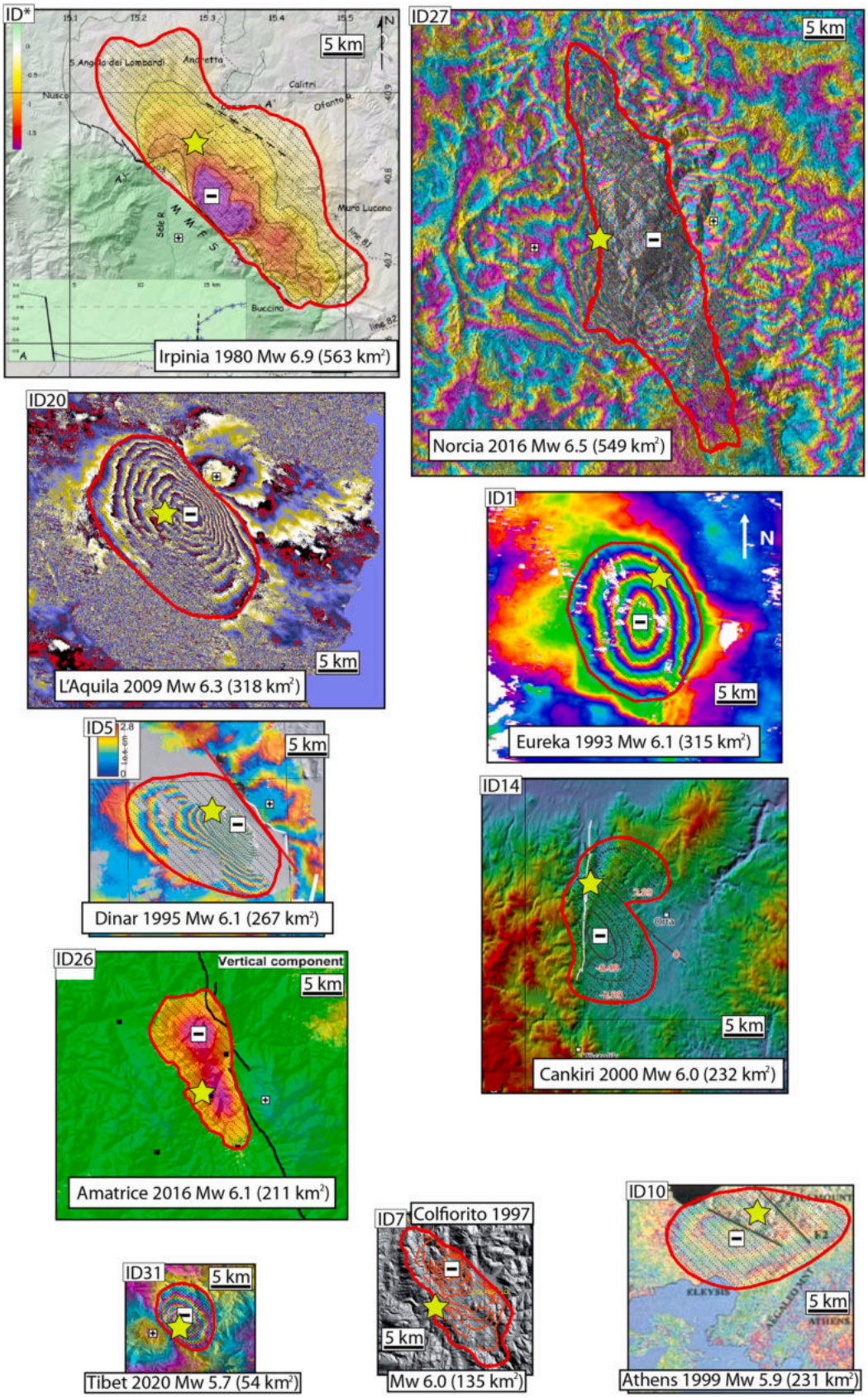

Fig. 2. InSAR images used for area computation of normal faults-related earthquakes. The area with concentrated vertical ground deformation is contoured by the solid line with internal dashed black lines. It is computed where more than a single interference fringe occurs. The area increases with magnitude. Notice that epicenters (yellow stars) are misplaced with respect to the maximum surface subsidence (−) where the larger shaking is expected. ID*, normal fault M 6.9 Irpinia 1980 area has been computed by geodetic leveling. (For interpretation of the references to colour in this figure legend, the reader is referred to the web version of this article.)

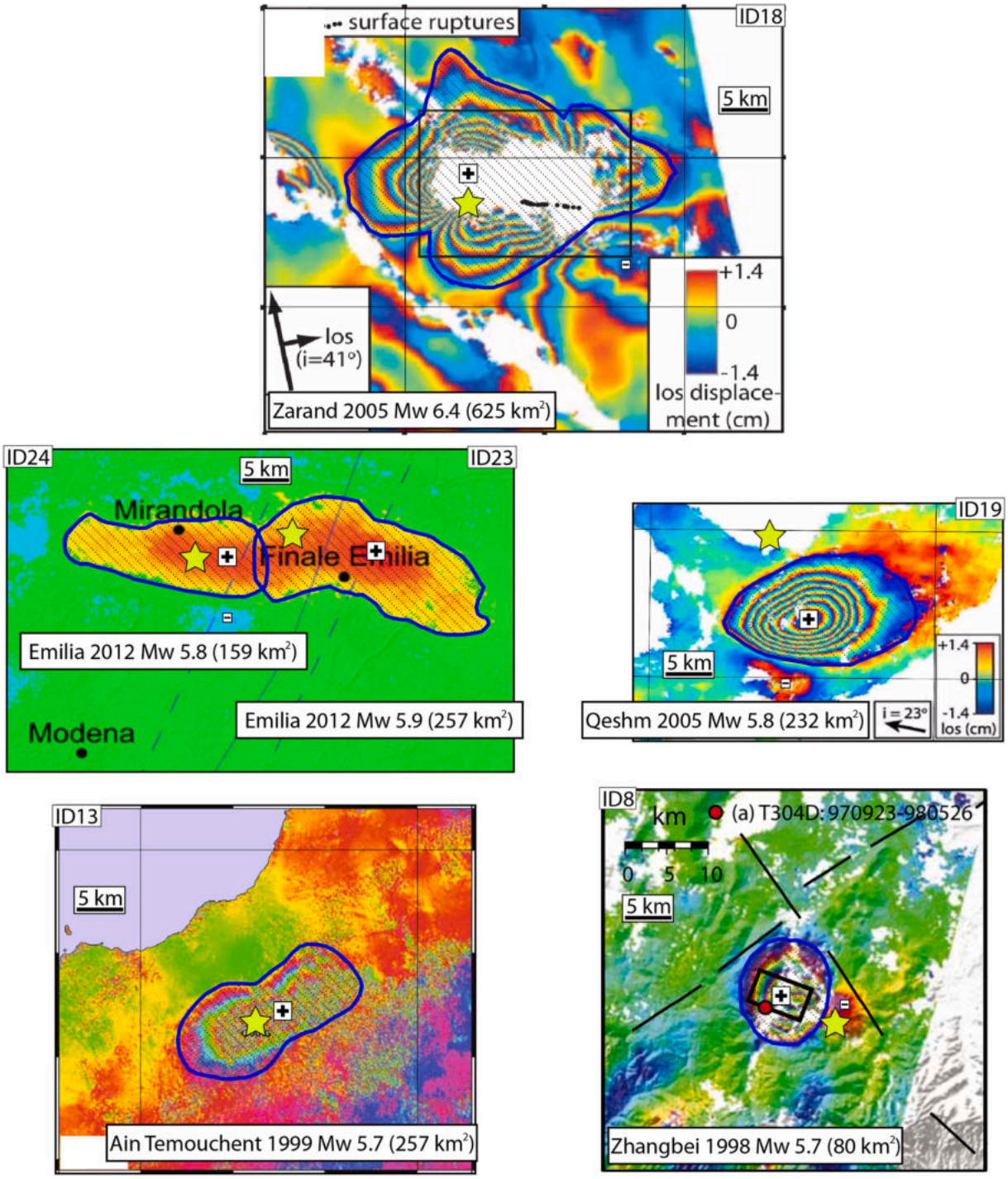

Fig. 3. InSAR images used for area computation of thrust faults related earthquakes. The area with concentrated vertical ground deformation is contoured by the dashed line with internal black crosses. It is computed where more than a single interference fringe occurs. The area increases with magnitude. Notice that epicenters (yellow stars) are misplaced with respect to the maximum surface uplift (+) where the larger shaking is expected. (For interpretation of the references to colour in this figure legend, the reader is referred to the web version of this article.)

and thrust fault events (geometrically is not quantifiable for strike-slip faults) considering the deformed area as the base of an inverted prism multiplied to the maximum seismogenic depth (Fig. 6a). Since the epicentral area increases with earthquake magnitude, the same consequently occurs for the involved volumes. The estimated volumes compared with the observed magnitudes doubles by an increase of 0.5 point of magnitude for normal earthquakes or quadruples for thrust earthquakes (Fig. 6b). It follows that the deformed volume exponentially increases with increasing magnitude and is twice as high in case of thrust fault earthquakes as in the normal fault earthquakes.

Focusing on coseismic ground shaking, we analyzed available data recorded by the Italian accelerometric network for events that are also studied in terms of SAR and included in Table 1. Namely, they are: i) Colfiorito 1997 (Mw 6.0); ii) L'Aquila 2009 (Mw 6.3); iii) Emilia 2012 1st event (Mw 5.9); iv) Emilia 2012 2nd event (Mw 5.8); v) Amatrice 2016 (Mw 6.1); vi) Norcia 2016 (Mw 6.5). We analyzed the maximum PGA value of accelerometric waveforms recorded at the coseismic stage for each event as follows: i) maximum PGA of the horizontal and vertical

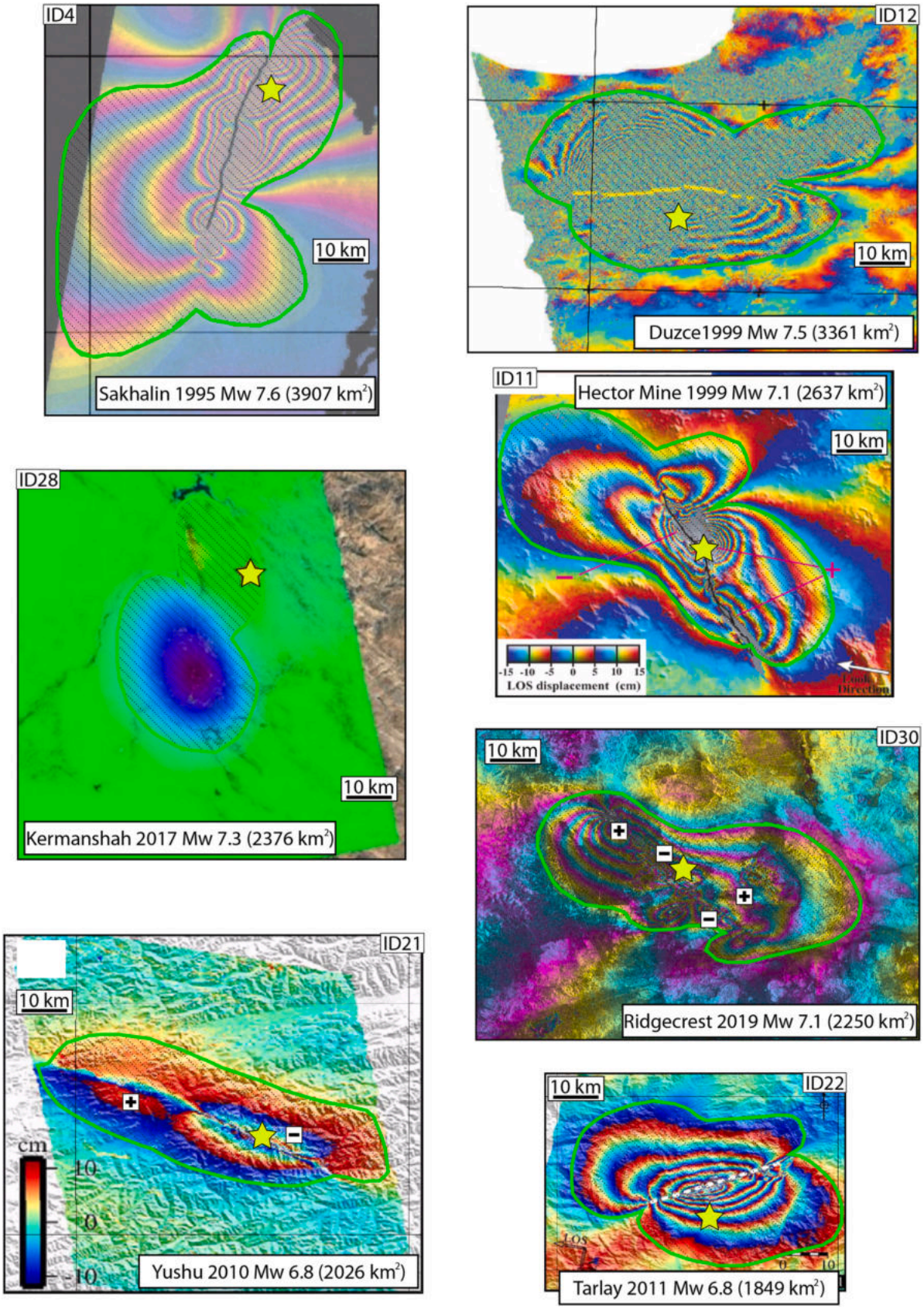

Fig. 4. InSAR images used for area computation for strike-slip faults-related earthquakes. The area with concentrated vertical ground deformation is contoured by the dashed line with internal black crosses. It is computed where more than a single interference fringe occurs. The area increases with magnitude. Notice that epicenters (yellow stars) are misplaced with respect to the maximum surface vertical deformation where the larger shaking is expected. (For interpretation of the references to colour in this figure legend, the reader is referred to the web version of this article.)

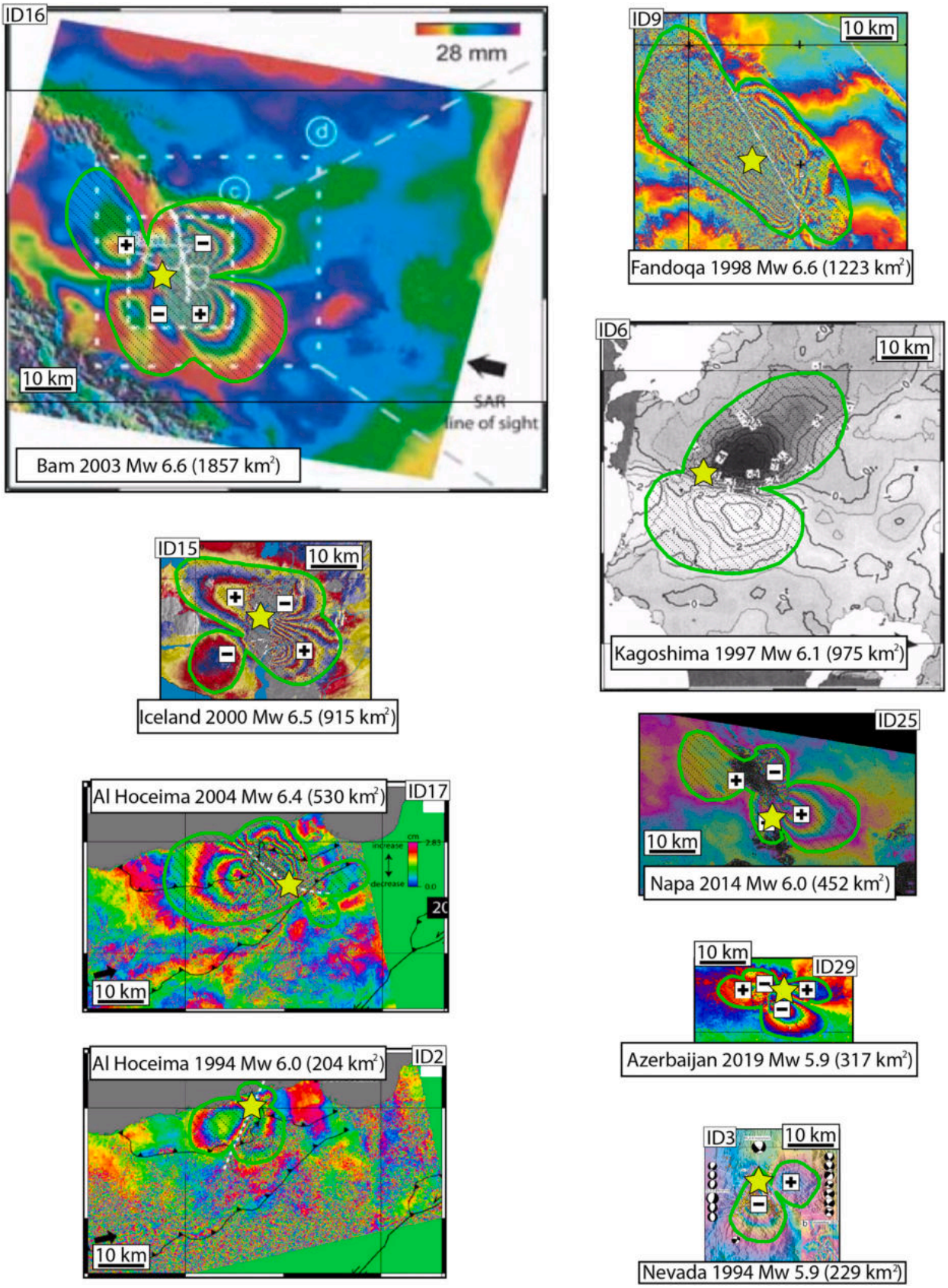

Fig. 4. (*continued*).

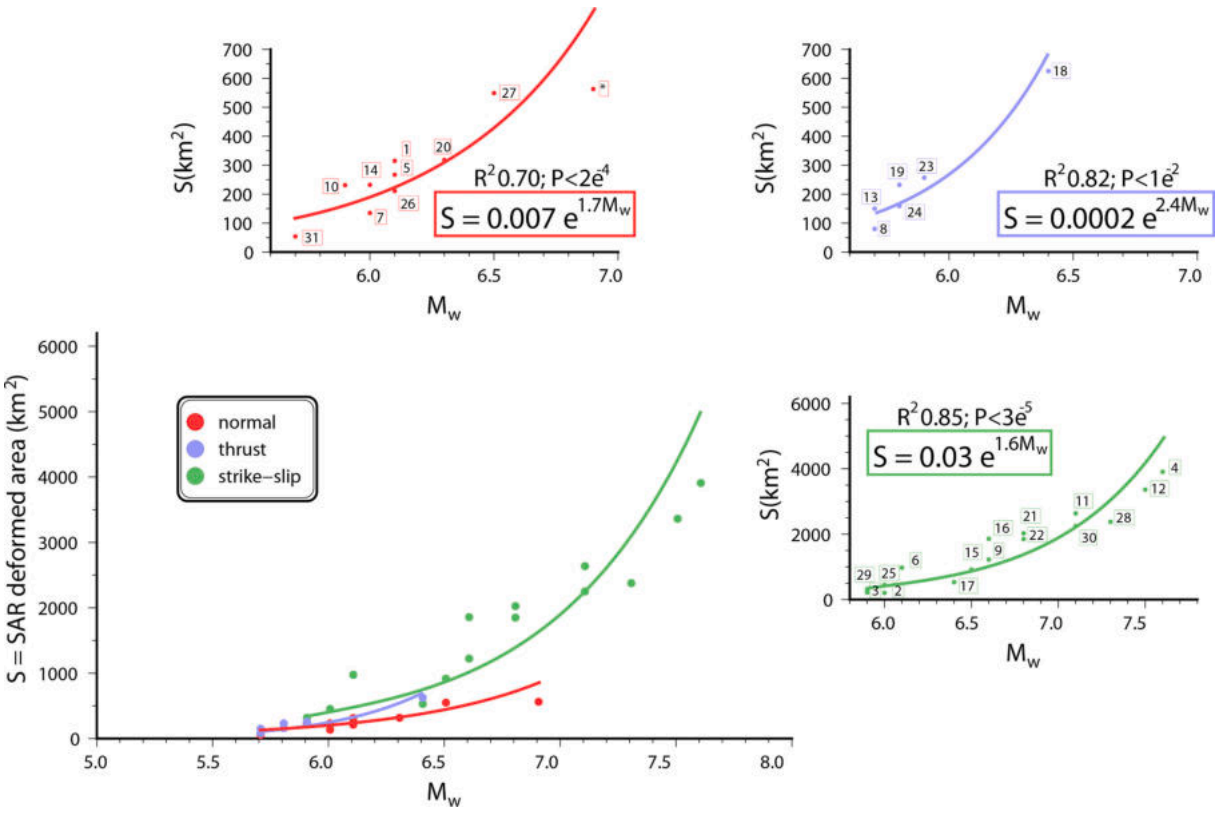

Fig. 5. Earthquake magnitude versus deformed area in the different tectonic settings. List of earthquakes in Table 1. The area (that represents at least the 90% of the mobilized rocks) affected by vertical (or LOS) movement increases with magnitude and appears to be larger for strike slip faults for a given magnitude.

components versus epicenter-station distance and versus the peak of maximum vertical deformation detected by InSAR (Fig. 7); ii) vertical-horizontal PGA ratio vs epicenter-station distance (Fig. 8). Plotted data have attached information about the soil category to take into account site effects of seismic attenuation/amplification from our analysis. The Emilia 2012 1st event has no accelerometric stations inside the polygon delimiting the deformed area recognized by SAR data, hence is not reported in the figures. We classified accelerometric stations in two categories: those lying within the polygon that encloses the deformed area recognized by SAR analysis, i.e., the InSAR epicentral area (red dots in Fig. 7) and those that fall outside the same polygon but within 35 km away (radial distance) from the epicenter (blue dots in Fig. 7). The chosen radius represents the long axis of the uplifted ellipse detected by InSAR.

The selected limit of 35 km, at least applied to our dataset, is a conservative limit that is situated far beyond the inflection of the data following the attenuation of the maximum PGA values. This is clear looking at Fig. 7, where the observations flatten along a horizontal line at a distance between 10 and 25 km from the depocenter/epicenter. Noteworthy, in most cases the seismic epicenter does not coincide with the area affected by the largest vertical (or quasi-vertical) motion here referred to as the depocenter; the latter is rather the area where the strongest shaking occurs and between the two areas the misfit may be even tens of km. Both the vertical and horizontal components of the maximum PGA always increase approaching the depocenter (Fig. 7a-e). An exception would seem to concern the case of Emilia 2012 second Mirandola event (Fig. 7c), but it should be noted that the observed trend here is masked because the area of highest positive LOS mostly coincides to the epicenter due to the overlap with the first Finale Emilia mainshock (Fig. 3). The increase of the maximum PGA recorded moving toward the epicenter is also observed (Fig. 7f-j). The only exception is represented by Norcia 2016 (Fig. 7f). The closest stations to the epicenter (< 5 km) recorded relatively low values of PGA (300–400 cm/s2) than the furthest ones (up to 900 cm/s2). This observation is a clear indication that the largest motion during the coseismic phase affected the depocenter instead of the epicenter. Regardless of the reference used for the distance, the stations record peak ground accelerations (PGA) 2–3 times greater within the epicentral fingerprint identified by the InSAR (red and light-red symbols in Fig. 7) than outside (blue and light-blue symbols in Fig. 7). Stations at the same distance from the reference point but inside or outside the epicentral fingerprint respectively clearly highlight this difference for Norcia (Fig. 7a and f), Emilia (Fig. 7c) and L'Aquila (Fig. 7d). Local effect of site amplification can be excluded from our observations because, apart from the case of Colfiorito 1997, the bedrock characteristics (discriminated through capital letters in Figs. 7 and 8) are homogeneous within the sub-network considered for each event.

Comparing PGA components recorded at the same station emerges that their ratio leans toward the vertical direction of the coseismic ground acceleration (Fig. 8). Considering records from accelerometric stations placed within the epicentral area (red and light-red points in Fig. 8), the ratio between the vertical and both the horizontal components (east and north) is in most cases >1. The ratio shows values up to 2 for normal fault earthquakes (Norcia 2016) or 4 for thrust fault earthquakes (Emilia 2012) indicating that the vertical acceleration rules the ground shaking when we are facing dip-slip faults. There is geographical correlation between the sites marked in red of Figs. 7 and 8 and the epicentral area of Figs. 2 to 4, because those sites are inside the epicentral area marked by the InSAR fingerprint. The blue signs pertain to the area outside the near-field. Some of the sites external to the epicentral area may also have experienced amplification. Nevertheless, there is a clear signature when comparing the PGA in and out the epicentral area delimiting the active domain by means of the vertical (or quasi-vertical LOS) ground displacement recorded by InSAR data. The misfit between the dominant vertical motion and the epicenter of the Italian earthquakes is in Fig. 9. In fact, the epicenter is where the rupture

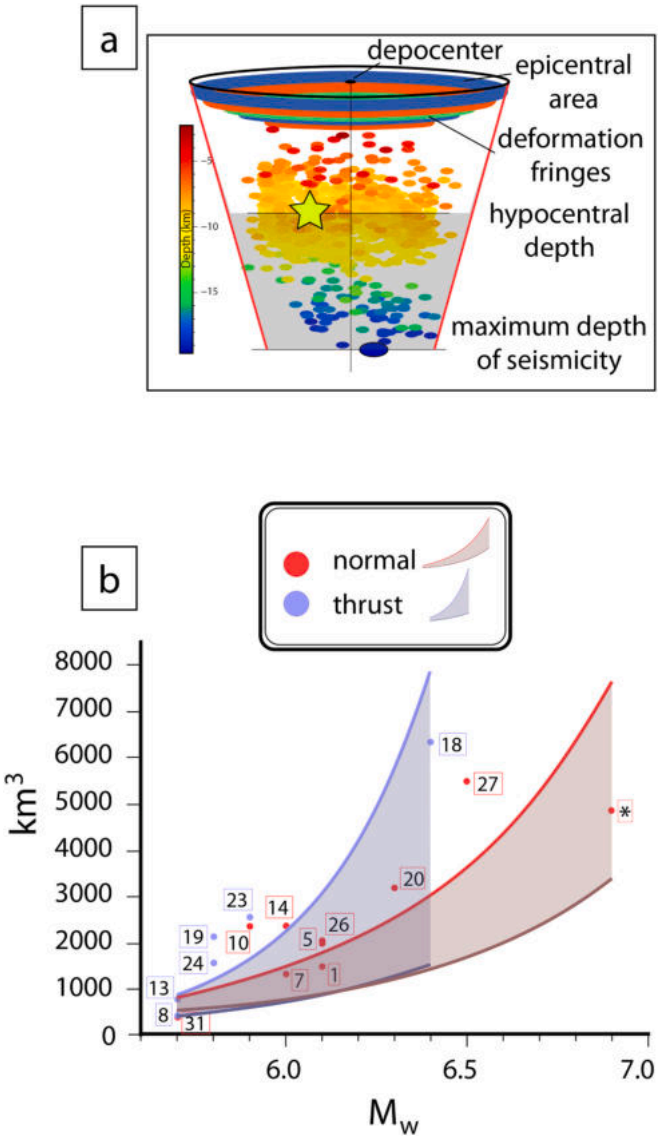

Fig. 6. Computation of volumes versus magnitude starting from InSAR data for a number of events shown in Fig. 1 and Table 1. For each event it has been selected the seismicity falling into the epicentral area detected by InSAR from 1979 to 2020, having <20 km maximum depth. The volume has been computed as illustrated in the text assuming an overturned prism with apex at depth and base at the Earth's surface (inset). The volume has been computed both with the whole seismicity (colored line) and from the hypocentral depth only (gray line), showing how the hypocenter is generally shallower than the real involved volume.

starts, before propagating far away, so that the slip peak and stronger impact can be somewhere else.

Nowadays it's well known that the epicenter is often located at the slip distribution margins; moreover, seismological data (mostly recorded in the far-field) are affected by higher uncertainties than InSAR data, perfectly covering the near-field. We often see the epicenter at the margin of the InSAR deformation, therefore finding the maximum shaking above the maximum slip along the fault plane is expected, or adjacent to the tip lines of strike-slip faults. In fact, we show that the maximum shaking is where the vertical component is larger. Therefore, we stress that the highest seismic hazard quantified by the PGA is where is the highest vertical coseismic deformation, where horizontal shaking can be more effective. This implies that the largest seismic hazard is not specifically along the fault, but where the ground is moving up or down the most.

According to the data of Table 1, the coseismic vertical maximum displacement (either uplift or subsidence) for a given magnitude tends to be larger for normal faults (Fig. 10) due to the steeper fault dip (Fig. 11) as proposed by Bignami et al. (2020). The depth of the brittle-ductile transition (BDT) controls the thickness of the seismogenic layer in all tectonic settings. However, Schorlemmer et al. (2005) have shown that earthquakes in extensional settings have lower magnitude than contractional tectonic environments, having a higher b-value (1.1) of the global Gutenberg-Richter law (b-value=1). This is consistent with the smaller volumes activated in extensional settings which determine smaller fault surfaces coseismic activation. In fact, along rift zones, the length of the mobilized volume depends on the seismogenic depth, which can be either the BDT or a low-angle detachment, and the ratio between the volume length and the seismogenic depth tends to be around 3 ± 1 (Fig. 12), whereas it may raise to 10 in strike-slip settings, and it can increase to more than 25 at the interface of subduction zones in contractional settings (Doglioni et al., 2015a). Moreover, the dip of thrusts and normal faults control the magnitude because the volume is moving respectively against or in favour of gravity (Fig. 13).

4. Discussion

SAR interferometry technique is a powerful tool for identifying and clearly delineating the most shaken area corresponding to the so-called near-field. In all tectonic environments, the fringe replicas mimic sort of fingerprints of the occurred earthquake. The recognized epicentral area or near-field has routinely an elliptic shape for thrust and normal faults, whereas it tends to quadrilobated around strike-slip faults (Figs. 2–4). The ratio between the long and short axis of the ellipse increases with magnitude in all tectonic settings. For thrust or normal faults, it coincides with the surface projection of the upper crustal volume that has been mobilized in the hanging wall (Fig. 6a). The deformed epicentral area is determined by the volume size and the related fault length, depth and dip. The thrusts have the largest near-field areas because they may affect bigger volumes, up to several hundred km long, not only because they have lower dip, but because they can have much higher magnitude. In fact, they may generate the strongest and most damaging earthquakes and tsunamis. Notice that in case of normal fault, adjacent to the subsided ground, it occurs an elongated ellipse where the ground has rather uplifted, but on average ten times less in volume (e.g., Bignami et al., 2019). Similarly, but with opposite sign, this occurs along thrust faults where the epicentral area is rather characterized by ground uplift and an adjacent elongated ellipse with much smaller subsidence. Therefore, we consider as active volume the upper crust where the vertical deformation is concentrated, regardless of it is the hanging wall of thrust or normal fault, or the volume adjacent in both sides of a subvertical strike-slip fault. The most deformed volume tends to be rather double lobate or quadrilobated on the two walls of sub vertical strike-slip faults, being the uplifted ground concentrated on the two opposite sides close to the tip lines where the crust converges, and vice versa the subsided ground where the crust diverges. The surface expression of the active volume can be defined as the active domain where the maximum earthquake intensity is expected. The surrounding passive volume may rather be considered as the passive domain.

Unlike the common assumption that the near-field is referred to the distance from the epicenter and from the fault, here we show that the largest shaking is not necessarily along the fault, but where the cumulate ground deformation recorded by InSAR has been maximum (Fig. 14). The drastic lowering of the PGA outside the fingerprint area explains why the macroseismic intensity drops rapidly outside this area, apart from local site amplifications. This is a well-established information that is quantified by the GMPE (e.g., Graizer and Kalkan, 2016). The high PGA values within the epicentral area can be controlled by the larger vertical oscillations of the crustal volume in the fault hanging wall, allowing horizontal shaking exerted by the seismic waves to be much more efficient in dislocating and shearing rocks; having a larger degree

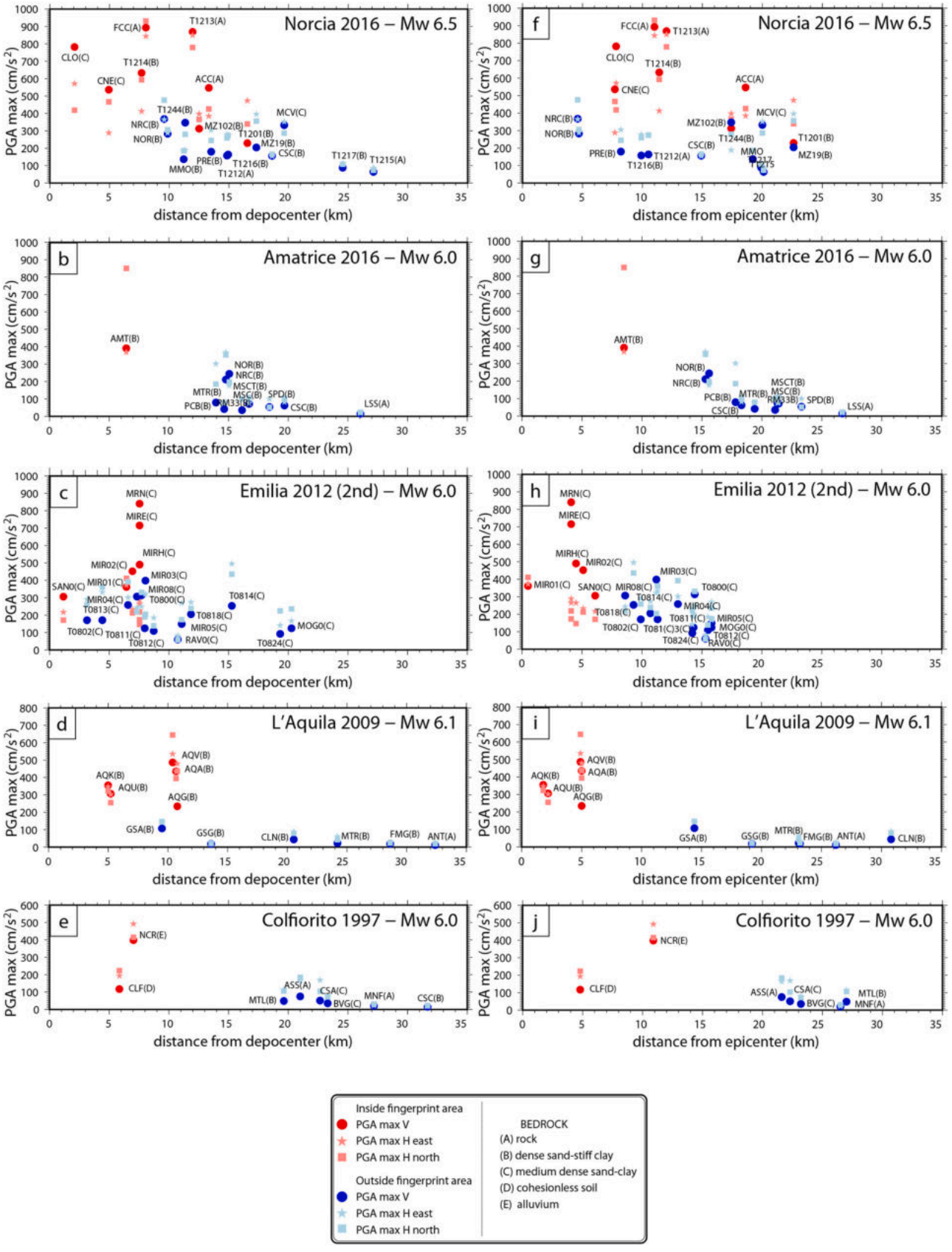

Fig. 7. Absolute PGA data. Vertical and horizontal PGA versus distance from the epicenter (a-e) or from the depocenter (f-j) of selected Italian earthquakes, comparing the area inside (red dots) and outside (blue dots) the epicentral area. Notice that the highest values coincide with the area depicted by InSAR as the most vertically deformed zone. (For interpretation of the references to colour in this figure legend, the reader is referred to the web version of this article.)

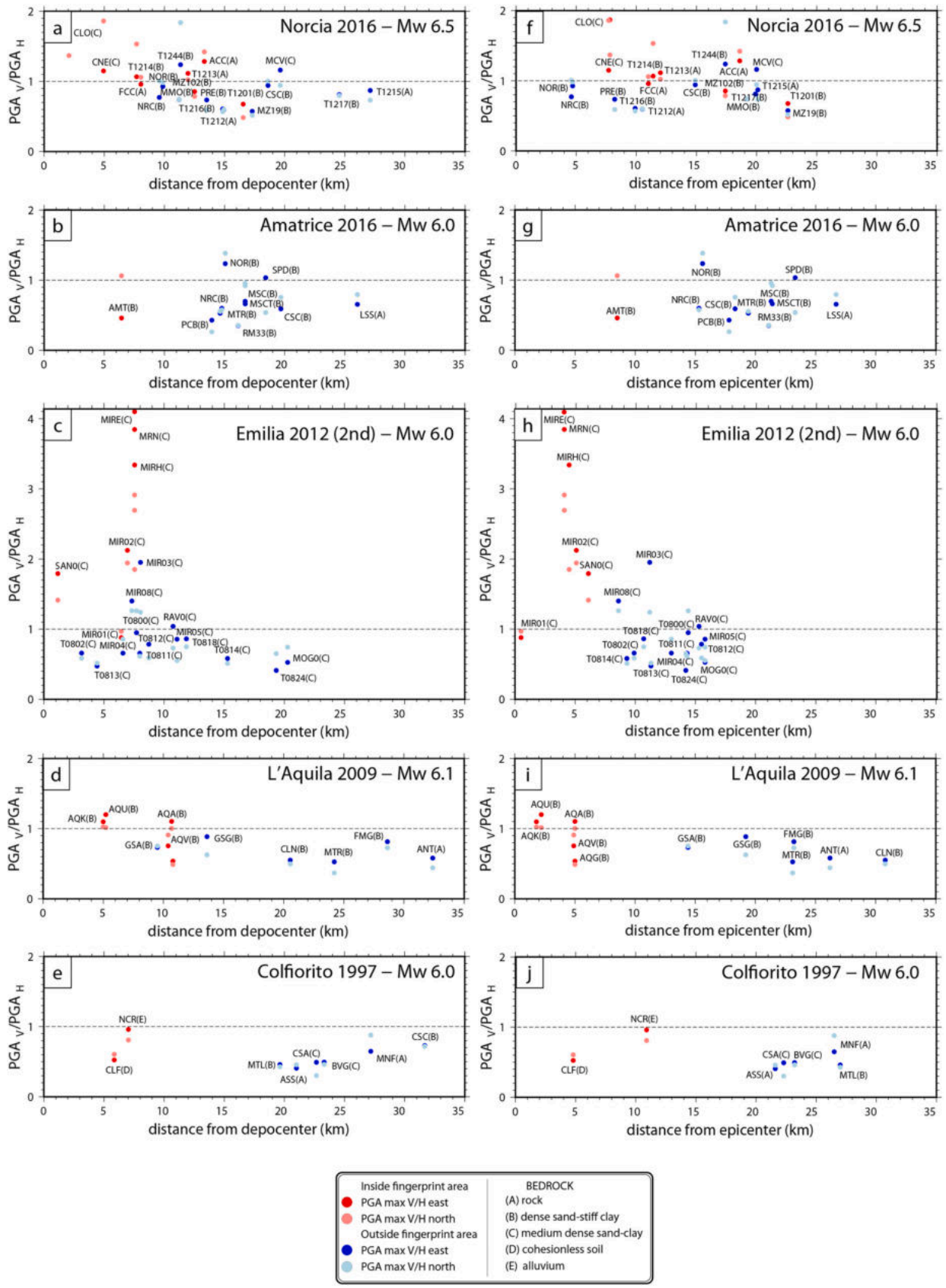

Fig. 8. Vertical-horizontal PGA ratio. Ratio of accelerations versus distance from the depocenter (a-e) or from the epicenter (f-j) of selected Italian earthquakes, comparing the area inside (red dots) and outside (blue dots) the epicentral area. Notice the ratio > 1 within the epicentral area illuminated by InSAR, pointing out the importance of the vertical motion within the near-field area. (For interpretation of the references to colour in this figure legend, the reader is referred to the web version of this article.)

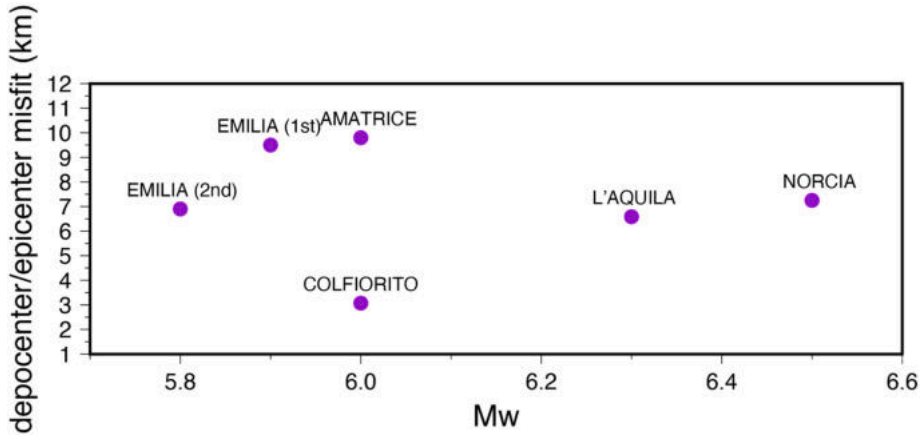

Fig. 9. Misfit of the recent Italian earthquake epicenters and the location of the highest vertical deformation recorded by InSAR data where the strongest shaking is inferred.

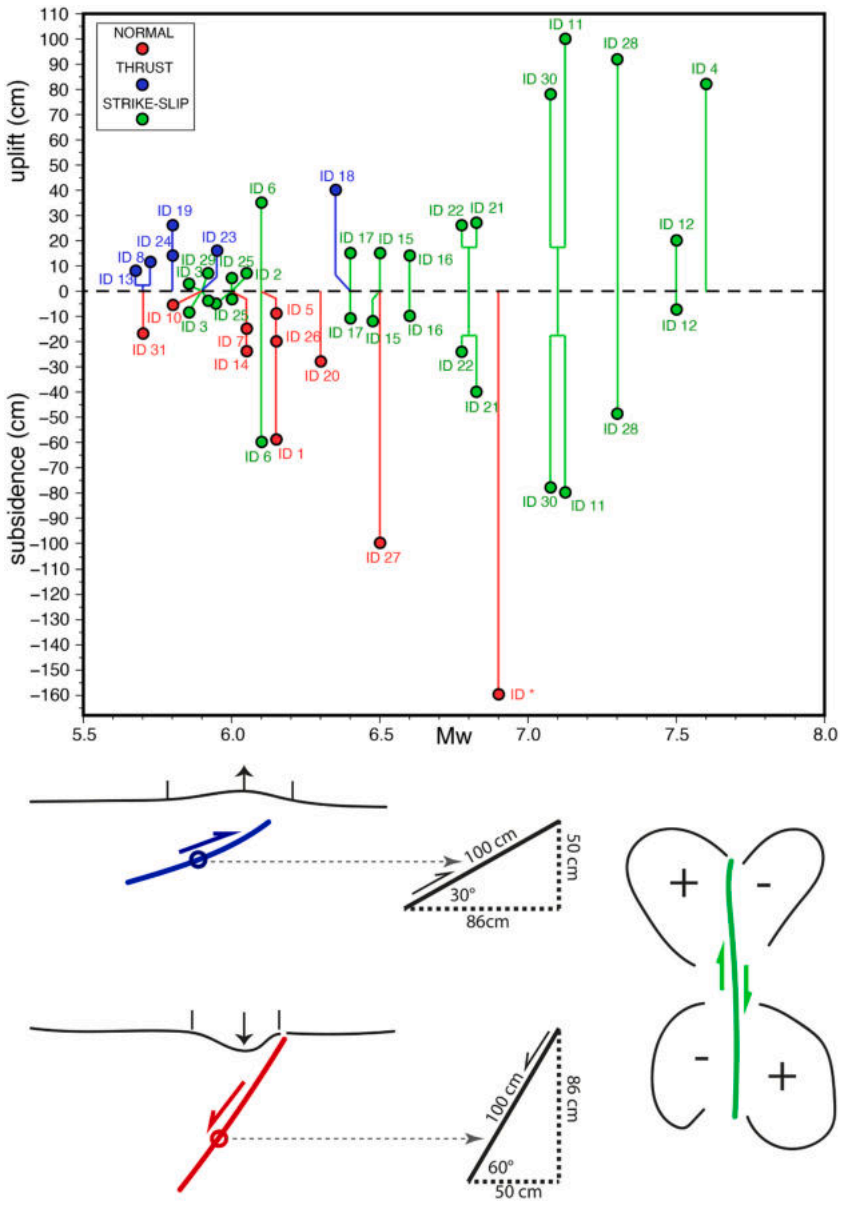

Fig. 10. Maximum vertical displacement of the 32 events analyzed versus magnitude. Notice that coseismic subsidence is slightly higher for normal faults with respect to thrusts uplift. The opposite occurs for area dimension as shown in Fig. 5. This can be related to the steeper dip of normal faults where the downward motion is governed by gravity (graviquake), whereas thrusts are moved upward by elastic rebound against gravity (elastoquake). See Table 1 for source data and event numbers.

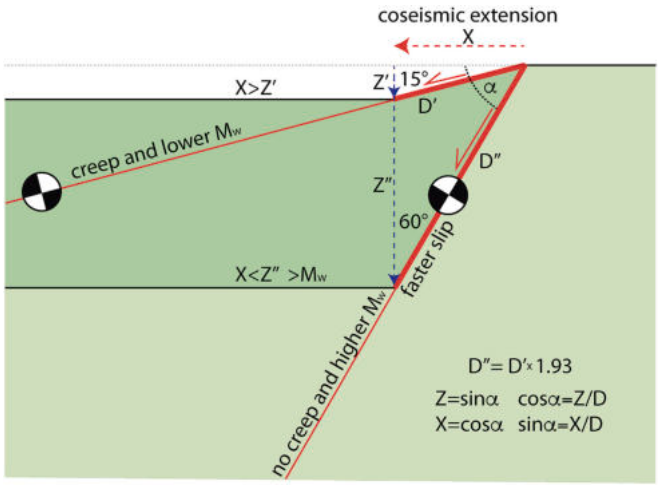

Fig. 11. Assuming a coseismic horizontal extension X, the vertical component varies as a function of the dip (α) of the normal fault. Two cases are shown, a 15° and 60° respectively. The vertical component Z' of 15° is smaller than the horizontal motion, whereas with a fault dip of 60° the vertical component Z" is larger than X. X = Z if the fault dip is 45°. The fault displacement of the 15° (D′) is about half of the 60° (D″). The low dip is usually a consequence of low friction rocks and is associated to creeping faults generating low magnitude earthquakes. During coseismic stage, the small slip and vertical component determine slower slip. The steeper dip is rather related to high friction lithologies, low or no creep and higher magnitude seismicity. This can be explained by the longer vertical component (Z") and higher gravitational potential, the larger displacement (D″) which also imply a faster motion along the fault. This framework is consistent with the mechanical constraints given by the vertical σ1 dominating the source of energy, i.e., gravity within an extensional tectonic setting (modified after Bignami et al., 2020).

of freedom, especially during the lowering of the ground, i.e., decreasing the acceleration of gravity, the horizontal acceleration and velocity can be more effective in oscillating the crustal volume and the masonry houses relying on it (Liberatore et al., 2019). Despite the larger areas strike-slip faults do not provide large vertical deformation and consequently, even the vertical and horizontal PGA may be lower than expected (Schmedes and Archuleta, 2008).

Ground deformation and seismic induced landslides are concentrated in the hanging wall of normal faults (Martino et al., 2014), where in fact SAR data show the strongest vertical coseismic deformation and accelerometric data are more intense. Wilkinson et al. (2017) have shown that the surface coseismic rupture and subsidence in the hanging wall is related to the normal fault activated by the 2016 Mw 6.5 Norcia earthquake in central Italy. They also have shown the independence of the vertical collapse of the hanging wall volume of the normal fault and the generation of seismic waves propagating across the hanging wall a few seconds later, while the volume was still moving. Therefore, during an earthquake, the hanging wall volume is subject to two separate phenomena consisting of the vertical and horizontal motions imposed by the tectonic setting, and the shaking generated by the seismic waves sourced by the fault plane (P- and S-waves). These effects overlap in the hanging wall and can be defined as the coseismic active volume where the largest oscillations and surface damages occur. This mechanism may be referred to the constructive interference of waves, where the sum of the two amplifies the oscillation (Fig. 14). This phenomenon was usually inferred for the interference of seismic waves (e.g., S-waves and Rayleigh waves, Kawase, 1996). Here we expect a further different interference of the moving hanging wall volume crossed by the whole train of seismic waves (P, S, surface waves) generated all along the fault plane. Within this volume and at the Earth's surface where seismic waves are reflected (and even locally amplified), the ground shaking is maximum. This area corresponds to the active domain. Outside the coseismically mobilized hanging wall volume, the seismic waves interact with a more static upper crust and the resulting shaking is much lower, hence the rapid decrease of peak ground acceleration and velocity outside this area

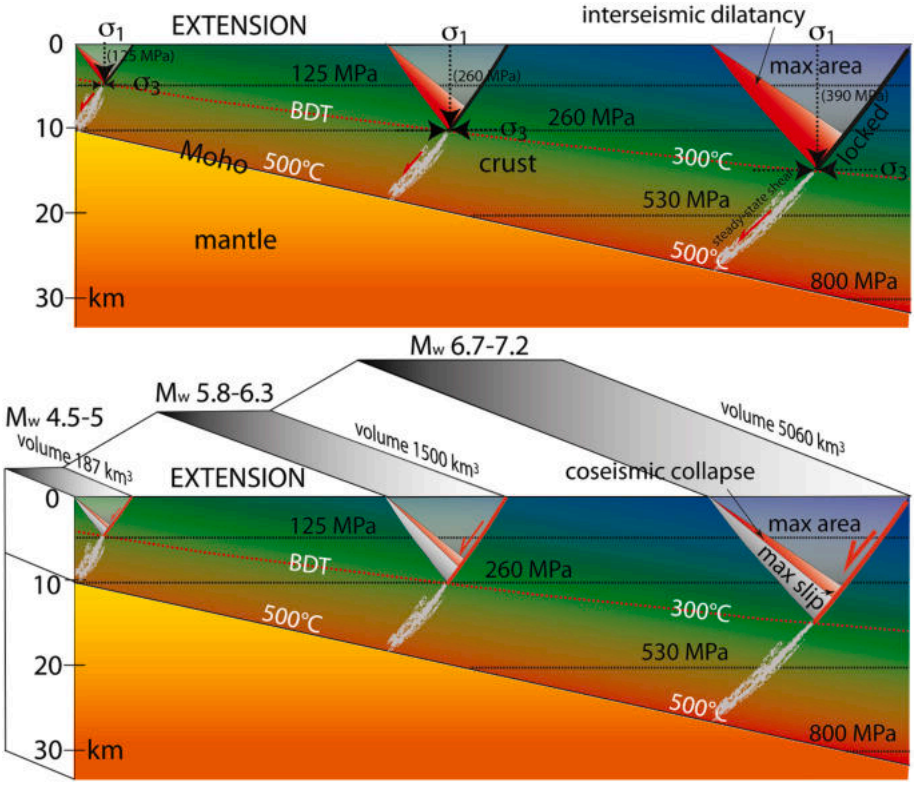

Fig. 12. In extensional tectonic settings, the ratio between the seismogenic layer depth and the hanging wall length appears to be, in average, 3 ± 1. As the thickness increases, the volume enlarges, the fault is longer, and the hanging wall collapse determines a greater fault slip and a consequent higher earthquake magnitude. Note that doubling the seismogenic layer from 5 to 10 km, the volume increases about 1 order of magnitude, as the maximum earthquake size, from M5 to M6. BDT, brittle-ductile transition. The red wedges in the section above suggest the inferred dilated crustal volume permeated by thousands of millimetric microfractures (modified after Bignami et al., 2020). Therefore, the deeper the BDT, the bigger the volume and magnitude of the earthquake, and the larger the area affected by coseismic subsidence. (For interpretation of the references to colour in this figure legend, the reader is referred to the web version of this article.)

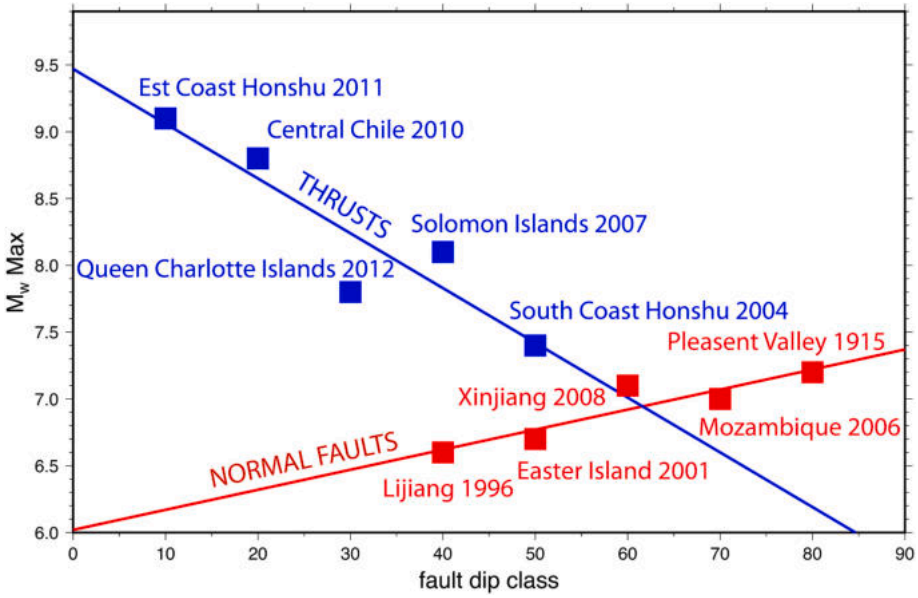

Fig. 13. Comparison between thrust-related (blue) and normal fault earthquakes (red) versus fault dip. The magnitude decreases with dip for thrusts, whereas it increases along normal faults. This opposite behavior supports different energy supply for the two tectonic settings, i.e., elastic rebound for moving the hanging wall upward against gravity, and gravitational potential for normal faults (modified after Bignami et al., 2020). (For interpretation of the references to colour in this figure legend, the reader is referred to the web version of this article.)

as described by the ground motion prediction equations (GMPE) in the adjacent passive volume, where the vertical and horizontal kinematics tend to zero moving away from the epicentral area (e.g., Graizer and Kalkan, 2016 and references therein) due to the anelasticity of the Earth's crust that tends to buffer the energy dissipated by the seismic waves. This area can be classified as the passive domain.

Wilkinson et al. (2017) show that the surface coseismic displacements associated to the 2016 Mw 6.5 Norcia event occurred about 2–3 s after the earthquake origin time and the main slip took place in 2–3 s while the ground started shaking, being the PGA at about 6 s after the origin time. Their GNSS data show that the ground continued to oscillate for about 10–15 s. The displacement represents the most surficial expression of the slip initiated at the hypocenter, but seismic waves originate along the fault plane at 8–9 km depth and need few seconds to reach the surface. This is especially true for S and Rayleigh waves that are slower. Within the lower hanging wall volume, its downward motion should have been contemporaneous to the passage of seismic waves, where we can infer the trapped waves to be originated and the constructive interference to occur. Therefore, the downward motion occurred contemporaneously to the passage of seismic waves, supporting the coexistence of the two phenomena and the relative interference within the active volume.

Therefore, InSAR images depict quite precisely the dimension and shape of the epicentral area, the volume and the related faults that moved during a seismic sequence, also helping the discrimination between the two fault planes provided by seismological data, thus identifying the fault where ruptures occur. The fingerprint of the so-called near-field is larger than 100 km^2 for M6 earthquakes, a dimension definitely too large to be neglected for seismic hazard assessments. In fact, unlike common practice the hazard maps should be calibrated for the near-field where the stronger shaking is expected to occur. We did not fully recognize the increase of misfit between epicenter and depocenter with magnitude, possibly because there are not enough InSAR data set, and errors in the estimation of the fingerprint extent, plus the incertitude of the epicenters, especially in remote areas where the seismic stations are scarce. With a given fault slip along dip, the coseismic vertical downward component is higher for normal faults, and lower vertical uplift for thrusts due to the higher and lower fault dip respectively. Strike-slip faults, having mostly horizontal slip, have the lowest vertical coseismic component, mostly concentrated laterally to the tip lines. On the other hand, with the same amount of slip, thrust faults generate wider areas with respect to normal faults because of their lower fault dip. Therefore, assuming a given magnitude and similar slip, the vertical shaking should increase from strike-slip, thrust and normal fault, and the opposite for the horizontal shaking.

5. Conclusions

SAR interferometry technique allows identifying and clearly delineating the most shaked area corresponding to the so-called near-field. InSAR data figure out that the epicentral area or near-field has routinely an elliptic shape for thrust and normal faults, whereas it tends to quadrilobate around strike-slip faults, thus providing a fingerprint of the occurred earthquake. The ratio between the long and short axis of the ellipse increases with magnitude in all tectonic settings. In all tectonic settings, the dimension of the deformed epicentral area is determined by the vertical projection of the mobilized hanging wall (thrusts and normal faults) or adjacent (strike slip) that is related to the fault length, depth, and dip. Therefore, the coseismically deformed area increases exponentially with the magnitude size. The thrusts have the largest near-field areas because they may affect bigger volumes, up to several hundred km long. Unlike the common assumption that the near-field is referred to the distance from the epicenter and from the fault, here we show that the largest shaking is not necessarily along the fault, but where the cumulate ground deformation recorded by InSAR has been maximum and not always coincident with the epicenter (Fig. 14). Therefore, the larger shaking in the epicentral area or active domain (Fig. 15) is due to the regional vertical motion of the involved volume, besides the amplification site effects that may occur inside and even outside the active domain. Within the epicentral area, the fault hanging wall is subject to two unsolved physically separated and overlapping phenomena, i.e., i) the dynamic fall or uplift and ii) the shaking generated by the seismic waves due to the slip and related friction along the fault plane. The combination of these two actions occurs mainly only within the activated volume and the surface area of this volume is efficiently detected by InSAR data. We may define this as the active domain, being the surface projection of the active volume. Within the active domain further relevant phenomena occur, such as fault directivity and trapped waves that enhance the shaking (Calderoni et al., 2012, 2017). The crustal volume moving on the fault dictates the surface area. The measure of the area could practically be enough, but to understand the mechanism governing the volume and the consequent surface area, it depends on the tectonic style, the dip and depth of the activated fault plane. Therefore, the dimension of the epicentral area is

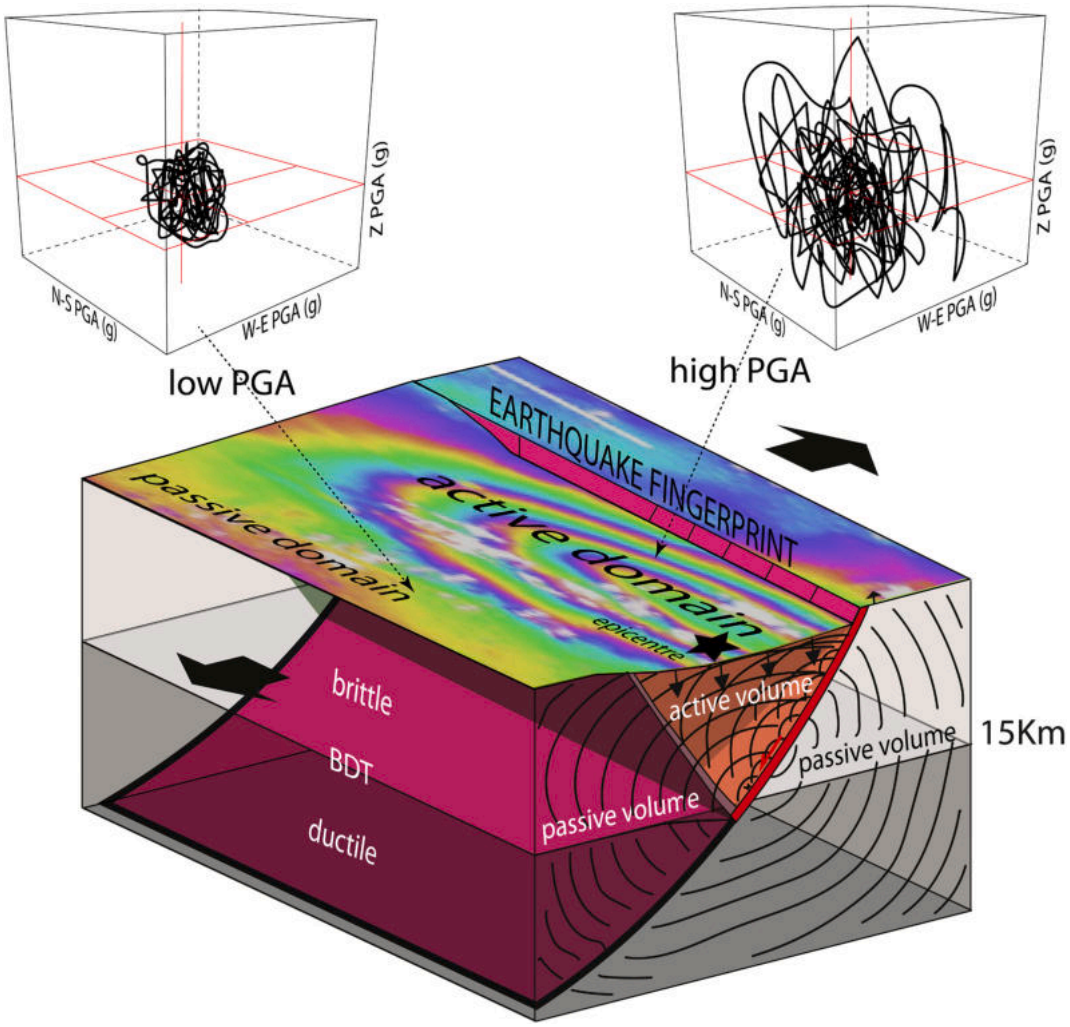

Fig. 14. Sketch illustrating the physical model. The coseismic ground deformation detected by InSAR data represents the fingerprint of the epicentral area and is located above the volume mobilized in the fault hanging wall in case of extensional setting. The area increases with magnitude. The earthquake epicenter is misplaced relative to the depocenter of the maximum coseismic subsidence where the strongest shaking is recorded. Outside the elongated epicentral area, even if relatively close to the epicenter, the vertical coseismic deformation is drastically reduced as well as the shaking; see the hypothetic trajectory of the acceleration vector inside and outside the epicentral area.

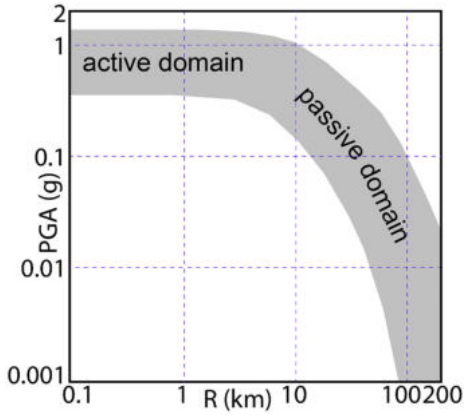

Fig. 15. Diagram of the PGA (g) average data in the gray area from the literature (see text) versus distance (R) inferring the active and passive domains.

well described by the InSAR data that illuminate the fingerprint of the so-called near-field. Being these areas larger than 100 km^2 for M6 earthquakes, the dimension is definitely too large to be neglected for seismic hazard assessments. Probabilistic seismic hazard maps have relevant limitations and serious methodological pitfalls (Stein et al., 2012; Magrin et al., 2017; Scholz, 2019). We suggest here that they should be calibrated for the near-field or active domain, i.e., the epicentral area (Grimaz and Malisan, 2014), where stronger shaking is expected to occur within it, not for the passive volume and the related passive domain, unless its local maximum hazard is lower with respect to the far-field effects of larger distal earthquakes. The computation of synthetic active domains of the future earthquakes may help to calibrate the seismic hazard assessment where the vertical motion plays a relevant role in enhancing larger horizontal shaking and greater damage.

Declaration of Competing Interest

None.

Acknowledgments

We thank Eugenio Carminati, Rita Di Giovambattista, Andrè Herrero, Domenico Liberatore, Pio Lucente and Giuliano Milana for fruitful discussions. The paper benefited by the review of Alik Ismail-Zadeh and two anonymous referees. We acknowledge institutional financial

support from Sapienza University of Rome, Italy (Ateneo 2018 grant). Shape files with georeferenced SAR images and vectorial polygons delimiting epicentral areas used in this study are available under request to PP. PGA data can be downloaded from the official repository at http://itaca.mi.ingv.it/ItacaNet_31/. Most figures were produced using the GMT software (http://gmt.soest.hawaii.edu/).

References

Akoglu, A.M., Cakir, Z., Meghraoui, M., Belabbes, S., El Alami, S.O., Ergintav, S., Akyüz, H.S., 2006. The 1994–2004 Al Hoceima (Morocco) earthquake sequence: conjugate fault ruptures deduced from InSAR. Earth Planet. Sci. Lett. 252 (3–4), 467–480. https://doi.org/10.1016/j.epsl.2006.10.010.

Albano, M., Barba, S., Bignami, C., Carminati, E., Doglioni, C., Moro, M., Stramondo, S., Saroli, M., 2021a. Three-dimensional numerical simulation of the interseismic and coseismic phases associated with the 6 April 2009, Mw 6.3 L'Aquila earthquake (Central Italy). Tectonophysics 798, 228685. https://doi.org/10.1016/j.tecto.2020.228685.

Albano, M., Barba, S., Bignami, C., Carminati, E., Doglioni, C., Moro, M., Saroli, M., Samsonov, S., Stramondo, S., 2021b. Numerical modeling of the seismic cycle for normal and reverse faulting earthquakes in Italy. Geophys. J. Int. 225, 627–645. https://doi.org/10.1093/gji/ggaa608.

Álvarez-Gómez, J.A., 2019. FMC—earthquake focal mechanisms data management, cluster and classification. SoftwareX 9, 299–307. https://doi.org/10.1016/j.softx.2019.03.008.

Ambraseys, N.N., Douglas, J., 2003. Near-field horizontal and vertical earthquake ground motions. Soil Dyn. Earthq. Eng. 23 (1), 1–18.

Amelung, F., Bell, J.W., 2003. Interferometric synthetic aperture radar observations of the 1994 Double Spring Flat, Nevada, earthquake (M5.9): main shock accompanied by triggered slip on a conjugate fault. J. Geophys. Res. Solid Earth 108 (B9). https://doi.org/10.1029/2002JB001953.

Anzidei, M., Boschi, E., Cannelli, V., Devoti, R., Esposito, A., Galvani, A., Melini, D., Pietrantonio, G., Riguzzi, F., Sepe, V., Serpelloni, E., 2009. Coseismic deformation of the destructive April 6, 2009 L'Aquila earthquake (Central Italy) from GPS data. Geophys. Res. Lett. 36 (17).

Atzori, S., Hunstad, I., Chini, M., Salvi, S., Tolomei, C., Bignami, C., Stramondo, S., Trasatti, E., Antonioli, A., Boschi, E., 2009. Finite fault inversion of DInSAR coseismic displacement of the 2009 L'Aquila earthquake (Central Italy). Geophys. Res. Lett. 36 (15) https://doi.org/10.1029/2009GL039293.

Bak, P., Christensen, K., Danon, L., Scanlon, T., 2002. Unified scaling law for earthquakes. Phys. Rev. Lett. 88, 178501–178504. https://doi.org/10.1103/PhysRevLett.88.178501.

Bath, M., 2013. Introduction to Seismology, 27. Birkhäuser.

Bath, M., Duda, S.J., 1964. Earthquake volume, fault plane area, seismic energy, strain, deformation and related quantities. Ann. Geofis. 17 (3), 353–368. https://doi.org/10.4401/ag- 5213.

Beaudouin, T., Bellier, O., Sebrier, M., 1994. Practical lessons from the Loma Prieta earthquake. Earthq. Eng. 28, 33–57.

Belabbès, S., Meghraoui, M., Çakir, Z., Bouhadad, Y., 2009. InSAR analysis of a blind thrust rupture and related active folding: the 1999 Ain Temouchent earthquake (M w 5.7, Algeria) case study. J. Seismol. 13 (4), 421–432. https://doi.org/10.1007/s10950-008-9135-x.

Berberian, M., Jackson, J.A., Fielding, E., Parsons, B.E., Priestley, K., Qorashi, M., Talebian, M., Walker, R., Wright, T.J., Baker, C., 2001. The 1998 March 14 Fandoqa earthquake (Mw 6.6) in Kerman province, southeast Iran: re-rupture of the 1981 Sirch earthquake fault, triggering of slip on adjacent thrusts and the active tectonics of the Gowk fault zone. Geophys. J. Int. 146 (2), 371–398. https://doi.org/10.1046/j.1365-246x.2001.01459.x.

Biggs, J., Wright, T.J., 2020. How satellite InSAR has grown from opportunistic science to routine monitoring over the last decade. Nat. Commun. 11 (1), 1–4.

Bignami, C., Valerio, E., Carminati, E., Doglioni, C., Tizzani, P., 2019. Volume unbalance on the 2016 Amatrice - Norcia (Central Italy) seismic sequence and insights on normal fault earthquake mechanism. Sci. Rep. 9, 4250. https://doi.org/10.1038/s41598-019-40958-z.

Bignami, C., Valerio, E., Carminati, E., Doglioni, C., Petricca, P., Tizzani, P., Lanari, R., 2020. Are normal fault earthquakes due to elastic rebound or gravitational collapse? Ann. Geophys. 63 (2), SE213, 2020. https://doi.org/10.4401/ag-8455.

Bignami, C., Antonioli, A., Atzori, S., Kiratzi, A., Polcari, M., Svigkas, N., Tolomei, C., Laboratory, G, 2021. Mapping InSAR deformation of low and moderate earthquakes. Proc. Comp. Sci. 181, 214–219. https://doi.org/10.1016/j.procs.2021.01.139.

Bondar, I., Storchak, D., 2011. Improved location procedures at the International Seismological Centre. Geophys. J. Int. 186, 1220–1244. https://doi.org/10.1111/j.1365-246X.2011.05107.x.

Bormann, P., Saul, J., 2020. Earthquake magnitude. In: Encyclopedia of Solid Earth Geophysics, pp. 2473–2496.

Burgmann, R., Ayhan, M.E., Fielding, E.J., Wright, T.J., McClusky, S., Aktug, B., Demir, C., Lenk, O., Turkezer, A., 2002. Deformation during the 12 November 1999 Duzce, Turkey, earthquake, from GPS and InSAR data. Bull. Seismol. Soc. Am. 92 (1), 161–171. https://doi.org/10.1785/0120000834.

Cakir, Z., Akoglu, A.M., 2008. Synthetic aperture radar interferometry observations of the M= 6.0 Orta earthquake of 6 June 2000 (NW Turkey): reactivation of a listric fault. Geochem. Geophys. Geosyst. 9 (8) https://doi.org/10.1029/2008GC002031.

Calderoni, G., Di Giovambattista, R., Vannoli, P., Pucillo, S., Rovelli, A., 2012. Fault-trapped waves depict continuity of the fault system responsible for the 6 April 2009 Mw 6.3 L'Aquila earthquake, Central Italy. Earth Planet. Sci. Lett. 323, 1–8.

Calderoni, G., Rovelli, A., Di Giovambattista, R., 2017. Rupture directivity of the strongest 2016–2017 Central Italy earthquakes. J. Geophys. Res. Solid Earth 122 (11), 9118–9131.

Cheloni, D., De Novellis, V., Albano, M., Antonioli, A., Anzidei, M., Atzori, S., Avallone, A., Bignami, C., Bonano, M., Calcaterra, S., Castaldo, R., Casu, F., Cecere, G., De Luca, C., Devoti, R., et al., 2017. Geodetic model of the 2016 Central Italy earthquake sequence inferred from InSAR and GPS data. Geophys. Res. Lett. 44 (13), 6778–6787. https://doi.org/10.1002/2017GL073580.

Dall'Asta, A., Dabiri, H., Tondi, E., Morci, M., 2021. Influence of time-dependent seismic hazard on structural design. Bull. Earthq. Eng. 19 (6), 2505–2529.

D'Amico, M., Felicetta, C., Russo, E., Sgobba, S., Lanzano, G., Pacor, F., Luzi, L., 2020. Italian Accelerometric Archive v 3.1 - Istituto Nazionale di Geofisica e Vulcanologia. Dipartimento della Protezione Civile Nazionale. https://doi.org/10.13127/itaca.3.1.

Doglioni, C., Barba, S., Carminati, E., Riguzzi, F., 2011. Role of the brittle-ductile transition on fault activation. Phys. Earth Planet. Inter. 184, 160–171.

Doglioni, C., Carminati, E., Petricca, P., Riguzzi, F., 2015a. Normal fault earthquakes or graviquakes. Sci. Rep. 5 (1), 1–12.

Doglioni, C., Barba, S., Carminati, E., Riguzzi, F., 2015b. Fault on-off versus strain rate and earthquakes energy. Geosci. Front. 6, 265–276. https://doi.org/10.1016/j.gsf.2013.12.007.

Fujiwara, S., Yarai, H., Ozawa, S., Tobita, M., Murakami, M., Nakagawa, H., Nitta, K., Rosen, P.A., Werner, C.L., 1998. Surface displacement of the March 26, 1997 Kagoshima Ken Hokuseibu earthquake in Japan from synthetic aperture radar interferometry. Geophys. Res. Lett. 25 (24), 4541–4544. https://doi.org/10.1029/1998GL900191.

Fukahata, Y., Wright, T.J., 2008. A non-linear geodetic data inversion using ABIC for slip distribution on a fault with an unknown dip angle. Geophys. J. Int. 173 (2), 353–364. https://doi.org/10.1111/j.1365-246X.2007.03713.x.

Galli, P., Peronace, E., 2014. New paleoseismic data from the Irpinia Fault. A different seismogenic perspective for southern Apennines (Italy). Earth Sci. Rev. 136, 175–201. https://doi.org/10.1016/j.earscirev.2014.05.013.

Graizer, V., Kalkan, E., 2016. Summary of the GK15 ground-motion prediction equation for horizontal PGA and 5% damped PSA from shallow crustal continental earthquakes. Bull. Seismol. Soc. Am. 106 (2), 687–707.

Grimaz, S., Malisan, P., 2014. Near-field domain effects and their consideration in the international and Italian seismic codes. Boll. Geofis. Teor. Appl. 55 (4).

Guglielmino, F., Anzidei, M., Briole, P., Elias, P., Puglisi, G., 2013. 3D displacement maps of the 2009 L'Aquila earthquake (Italy) by applying the SISTEM method to GPS and DInSAR data. Terra Nova 25 (1), 79–85. https://doi.org/10.1111/ter.12008.

Hernandez, B., Cocco, M., Cotton, F., Stramondo, S., Scotti, O., Courboulex, F., Campillo, M., 2004. Rupture history of the 1997 Umbria-Marche (Central Italy) main shocks from the inversion of GPS, DInSAR and near-field strong motion data. Ann. Geophys. 47 (4) https://doi.org/10.4401/ag-3349.

Iervolino, I., Spillatura, A., Bazzurro, P., 2018. Seismic reliability of code-conforming Italian buildings. J. Earthq. Eng. 22 (sup2), 5–27. https://doi.org/10.1080/13632469.2018.1540372.

Jónsson, S., Zebker, H., Segall, P., Amelung, F., 2002. Fault slip distribution of the 1999 M w 7.1 Hector Mine, California, earthquake, estimated from satellite radar and GPS measurements. Bull. Seismol. Soc. Am. 92 (4), 1377–1389. https://doi.org/10.1785/0120000922.

Kanamori, H., 1973. Mode of strain release associated with major earthquakes in Japan. Annu. Rev. Earth Planet. Sci. 1, 213–239.

Kawase, H., 1996. The cause of the damage belt in Kobe: "The basin-edge effect," constructive interference of the direct S-wave with the basin-induced diffracted/Rayleigh waves. Seismol. Res. Lett. 67 (5), 25–34.

Keylis-Borok, V.I., Malinovskaya, L.N., 1964. One regularity in the occurrence of strong earthquakes. J. Geophys. Res. 69 (14), 3019–3024. https://doi.org/10.1029/JZ069i014p03019.

Kontoes, C., Elias, P., Sykioti, O., Briole, P., Remy, D., Sachpazi, M., Veis, G., Kotsis, I., 2000. Displacement field and fault model for the September 7, 1999 Athens earthquake inferred from ERS2 satellite radar interferometry. Geophys. Res. Lett. 27 (24), 3989–3992. https://doi.org/10.1029/2000GL008510.

Kuang, J., Ge, L., Metternicht, G.I., Ng, A.H.M., Wang, H., Zare, M., Kamranzad, F., 2019. Coseismic deformation and source model of the 12 November 2017 Mw 7.3 Kermanshah Earthquake (Iran–Iraq border) investigated through DInSAR measurements. Int. J. Remote Sens. 40 (2), 532–554. https://doi.org/10.1080/01431161.2018.1514542.

Lavecchia, G., Castaldo, R., De Nardis, R., De Novellis, V., Ferrarini, F., Pepe, S., Brozzetti, F., Solaro, G., Cirillo, D., Bonano, M., Boncio, P., Casu, F., De Luca, C., Lanari, R., Manunta, M., Manzo, M., Pepe, A., Zinno, I., Tizzani, P., 2016. Ground deformation and source geometry of the 24 August 2016 Amatrice earthquake (Central Italy) investigated through analytical and numerical modeling of DInSAR measurements and structural-geological data. Geophys. Res. Lett. 43 (24), 12–389. https://doi.org/10.1002/2016GL071723.

Li, Z., Feng, W., Xu, Z., Cross, P., Zhang, J., 2008. The 1998 Mw 5.7 Zhangbei Shangyi (China) earthquake revisited: a buried thrust fault revealed with interferometric synthetic aperture radar. Geochem. Geophys. Geosyst. 9 (4) https://doi.org/10.1029/2007GC001910.

Liberatore, D., Doglioni, C., Al Shawa, O., Atzori, S., Sorrentino, L., 2019. Effects of coseismic ground vertical motion on masonry constructions damage during the 2016 Amatrice-Norcia (Central Italy) earthquakes. Soil Dyn. Earthq. Eng. 120 (2019), 423–435. https://doi.org/10.1016/j.soildyn.2019.02.015.

Magrin, A., Peresan, A., Kronrod, T., Vaccari, F., Panza, G.F., 2017. Neo-deterministic seismic hazard assessment and earthquake occurrence rate. Eng. Geol. 229, 95–109.
Mariani, M., Pugi, F., 2020. Jerk: Effetti Delle Azioni Sismiche Impulsive e Crisi Locali Nelle Strutture in Muratura. INGENIO. https://www.ingenio-web.it/27402-jerk-effetti-delle-azioni-sismiche-impulsive-e-crisi-locali-nelle-strutture-in-muratura.
Martino, S., Prestininzi, A., Romeo, R.W., 2014. Earthquake-induced ground failures in Italy from a reviewed database. Nat. Hazards Earth Syst. Sci. 14 (4), 799.
Massonnet, D., Feigl, K.L., 1995. Satellite radar interferometric map of the coseismic deformation field of the M= 6.1 Eureka Valley, California earthquake of May 17, 1993. Geophys. Res. Lett. 22 (12), 1541–1544. https://doi.org/10.1029/95GL01088.
Massonnet, D., Rossi, M., Carmona, C., Adragna, F., Peltzer, G., Feigl, K., Rabaute, T., 1993. The displacement field of the Landers earthquake mapped by radar interferometry. Nature 364 (6433), 138–142.
McGarr, A., 1999. On relating apparent stress to the stress causing earthquake fault slip. J. Geophys. Res. 104 (B2), 3003–3011.
Milana, G., Cultrera, G., Bordoni, P., Bucci, A., Cara, F., Cogliano, R., Di Giulio, G., Di Naccio, D., Famiani, D., Fodarella, A., Mercuri, A., 2019. Local site effects estimation at Amatrice (Central Italy) through seismological methods. Bull. Earthq. Eng. 1–27.
Monterroso, F., Bonano, M., Luca, C.D., Lanari, R., Manunta, M., Manzo, M., Onorato, G., Zinno, I., Casu, F., 2020. A global archive of coseismic DInSAR products obtained through unsupervised Sentinel-1 data processing. Remote Sens. 12 (19), 3189. https://doi.org/10.3390/rs12193189.
Nievas, C.I., Bommer, J.J., Crowley, H., van Elk, J., 2020. Global occurrence and impact of small-to-medium magnitude earthquakes: a statistical analysis. Bull. Earthq. Eng. 18, 1–35. https://doi.org/10.1007/s10518-019-00718-w.
Nissen, E., Yamini-Fard, F., Tatar, M., Gholamzadeh, A., Bergman, E., Elliott, J.R., Jackson, J.A., Parsons, B., 2010. The vertical separation of mainshock rupture and microseismicity at Qeshm island in the Zagros fold-and-thrust belt, Iran. Earth Planet. Sci. Lett. 296 (3–4), 181–194. https://doi.org/10.1016/j.epsl.2010.04.049.
Okada, Y., 1985. Surface deformation due to shear and tensile faults in a half-space. Bull. Seismol. Soc. Am. 75 (4), 1135–1154.
Okada, Y., 1992. Internal deformation due to shear and tensile faults in a half-space. Bull. Seismol. Soc. Am. 82 (2), 1018–1040.
Panza, G., Kossobokov, V.G., Peresan, A., Nekrasova, A., 2014. Why are the standard probabilistic methods of estimating seismic hazard and risks too often wrong. In: Earthquake Hazard, Risk and Disasters. Academic Press, pp. 309–357.
Pedersen, R., Jónsson, S., Árnadóttir, T., Sigmundsson, F., Feigl, K.L., 2003. Fault slip distribution of two June 2000 MW6. 5 earthquakes in South Iceland estimated from joint inversion of InSAR and GPS measurements. Earth Planet. Sci. Lett. 213 (3–4), 487–502. https://doi.org/10.1016/S0012-821X(03)00302-9.
Peyret, M., Chéry, J., Djamour, Y., Avallone, A., Sarti, F., Briole, P., Sarpoulaki, M., 2007. The source motion of 2003 bam (Iran) earthquake constrained by satellite and ground-based geodetic data. Geophys. J. Int. 169 (3), 849–865. https://doi.org/10.1111/j.1365-246X.2007.03358.x.
Polcari, M., Montuori, A., Bignami, C., Moro, M., Stramondo, S., Tolomei, C., 2017. An improved data integration algorithm to constrain the 3D displacement field induced by fast deformation phenomena tested on the Napa Valley earthquake. Computers & Geosciences 109, 206–215. https://doi.org/10.1016/j.cageo.2017.09.002.
Polcari, M., Palano, M., Moro, M., 2021. Performance evaluation of different SAR-based techniques on the 2019 ridgecrest sequence. Remote Sens. 13 (685) https://doi.org/10.3390/rs13040685.
Salvi, S., Stramondo, S., Cocco, M., Tesauro, M., Hunstad, I., Anzidei, M., Briole, P., Baldi, P., Sansosti, E., Fornaro, G., Lanari, R., Doumaz, F., Pesci, A., Lanari, R., 2000. Modeling coseismic displacements resulting from SAR interferometry and GPS measurements during the 1997 Umbria-Marche seismic sequence. J. Seismol. 4 (4), 479–499. https://doi.org/10.1023/A:1026502803579.
Schmedes, J., Archuleta, R.J., 2008. Near-source ground motion along strike-slip faults: insights into magnitude saturation of PGV and PGA. Bull. Seismol. Soc. Am. 98 (5), 2278–2290.
Scholz, C.H., 2019. The Mechanics of Earthquakes and Faulting. Cambridge University Press.
Schorlemmer, D., Wiemer, S., Wyss, M., 2005. Variations in earthquake-size distribution across different stress regimes. Nature 437 (7058), 539–542. https://doi.org/10.1038/nature04094.
Shearer, P.M., 2019. Introduction to Seismology. Cambridge University Press.
Stacey, F.D., Davis, P.M., 2008. Physics of the Earth. Cambridge University Press.
Stein, S., Wysession, M., 2009. An Introduction to Seismology, Earthquakes, and Earth Structure. John Wiley & Sons.
Stein, S., Geller, R.J., Liu, M., 2012. Why earthquake hazard maps often fail and what to do about it. Tectonophysics 562, 1–25.
Stramondo, S., Tesauro, M., Briole, P., Sansosti, E., Salvi, S., Lanari, R., Anzidei, M., Baldi, P., Fornaro, G., Avallone, A., Buongiorno, M.F., Franceschetti, G., Boschi, E., 1999. The September 26, 1997 Colfiorito, Italy, earthquakes: modeled coseismic surface displacement from SAR interferometry and GPS. Geophys. Res. Lett. 26 (7), 883–886. https://doi.org/10.1029/1999GL900141.
Stramondo, S., Chini, M., Bignami, C., Salvi, S., Atzori, S., 2010. X- C-, and L-band DInSAR investigation of the April 6, 2009, Abruzzi earthquake. IEEE Geosci. Remote Sens. Lett. 8 (1), 49–53. https://doi.org/10.1109/LGRS.2010.2051015.
Talebian, M., Biggs, J., Bolourchi, M., Copley, A., Ghassemi, A., Ghorashi, M., Hollingsworth, J., Jackson, J., Nissen, E., Oveisi, B., Parsons, B., Priestley, K., Saiidi, A., 2006. The Dahuiyeh (Zarand) earthquake of 2005 February 22 in Central Iran: reactivation of an intramountain reverse fault. Geophys. J. Int. 164 (1), 137–148. https://doi.org/10.1111/j.1365-246X.2005.02839.x.
Tizzani, P., Castaldo, R., Solaro, G., Pepe, S., Bonano, M., Casu, F., Manunta, M., Manzo, M., Pepe, A., Samsonov, S., Lanari, R., Sansosti, E., 2013. New insights into the 2012 Emilia (Italy) seismic sequence through advanced numerical modeling of ground deformation InSAR measurements. Geophys. Res. Lett. 40 (10), 1971–1977. https://doi.org/10.1002/grl.50290.
Tobita, M., Fujiwara, S., Ozawa, S., Rosen, P.A., Fielding, E.J., Werner, C.L., Murakami, M., Nakagawa, H., Nitta, K., Murakami, M., 1998. Deformation of the 1995 North Sakhalin earthquake detected by JERS-1/SAR interferometry. Earth Planets Space 50 (4), 313–325. https://doi.org/10.1186/BF03352118.
USGS, 2018. Why Do So Many Earthquakes Occur at a Depth of 10 km? Short Online Note. https://usgs.gov/faqs/why-do-so-many-earthquakes-occur-at-a-depth-of-10-km.
Valerio, E., Tizzani, P., Carminati, E., Doglioni, C., Pepe, S., Petricca, P., De Luca, C., Bignami, C., Solaro, G., Castaldo, R., De Novellis, V., Lanari, R., 2018. Ground deformation and source geometry of the 30 October 2016 Mw 6.5 Norcia earthquake (central Italy) investigated through seismological data, DInSAR measurements, and numerical modelling. Remote Sens. 10 (12), 1901. https://doi.org/10.3390/rs10121901.
Valerio, E., Manzo, M., Casu, F., Convertito, V., De Luca, C., Manunta, M., Monterroso, F., Lanari, R., De Novellis, V., 2020. Seismogenic source model of the 2019, Mw 5.9, East-Azerbaijan Earthquake (NW Iran) through the inversion of sentinel-1 DInSAR measurements. Remote Sens. 12 (8), 1346. https://doi.org/10.3390/rs12081346.
Wang, X., Liu, G., Yu, B., Dai, K., Zhang, R., Chen, Q., Li, Z., 2014. 3D coseismic deformations and source parameters of the 2010 Yushu earthquake (China) inferred from DInSAR and multiple-aperture InSAR measurements. Remote Sens. Environ. 152, 174–189. https://doi.org/10.1016/j.rse.2014.06.014.
Wang, X., Liu, G., Yu, B., Dai, K., Zhang, R., Ma, D., Li, Z., 2015. An integrated method based on DInSAR, MAI and displacement gradient tensor for mapping the 3D coseismic deformation field related to the 2011 Tarlay earthquake (Myanmar). Remote Sens. Environ. 170, 388–404. https://doi.org/10.1016/j.rse.2015.09.024.
Weston, J., Ferreira, A.M., Funning, G.J., 2012. Systematic comparisons of earthquake source models determined using InSAR and seismic data. Tectonophysics 532, 61–81. https://doi.org/10.1016/j.tecto.2012.02.001.
Wilkinson, M.W., McCaffrey, K.J., Jones, R.R., Roberts, G.P., Holdsworth, R.E., Gregory, L.C., Walters, R.J., Wedmore, L., Goodall, H., Iezzi, F., 2017. Near-field fault slip of the 2016 Vettore Mw 6.6 earthquake (Central Italy) measured using low-cost GNSS. Sci. Rep. 7 (1), 1–7.
Yao, H., Shearer, P.M., Gerstoft, P., 2012. Subevent location and rupture imaging using iterative back projection for the 2011 Tohoku Mw 9.0 earthquake. Geophys. J. Int. 190 (2), 1152–1168.
Yue, H., Lay, T., 2020. Resolving complicated faulting process using multi-point-source representation: iterative inversion algorithm improvement and application to recent complex earthquakes. J. Geophys. Res. Solid Earth 125 (2) e2019JB018601.